



HAL
open science

Wavelet Operators and Multiplicative Observation Models - Application to Joint Change-Detection and Regularization of SAR Image Time Series

Abdourrahmane Atto, Emmanuel Trouvé, Jean-Marie Nicolas, Thu Trang Le

► **To cite this version:**

Abdourrahmane Atto, Emmanuel Trouvé, Jean-Marie Nicolas, Thu Trang Le. Wavelet Operators and Multiplicative Observation Models - Application to Joint Change-Detection and Regularization of SAR Image Time Series. 2014. hal-00950823v2

HAL Id: hal-00950823

<https://hal.science/hal-00950823v2>

Preprint submitted on 28 Sep 2015 (v2), last revised 26 Jan 2016 (v3)

HAL is a multi-disciplinary open access archive for the deposit and dissemination of scientific research documents, whether they are published or not. The documents may come from teaching and research institutions in France or abroad, or from public or private research centers.

L'archive ouverte pluridisciplinaire **HAL**, est destinée au dépôt et à la diffusion de documents scientifiques de niveau recherche, publiés ou non, émanant des établissements d'enseignement et de recherche français ou étrangers, des laboratoires publics ou privés.

Wavelet Operators and Multiplicative Observation Models - Application to Joint Change-Detection and Regularization of SAR Image Time Series

Abdourrahmane M. ATTO^{1,*}, Emmanuel TROUVÉ¹, Jean-Marie NICOLAS², Thu-Trang LÊ¹

Abstract—This paper addresses the sparsity and stochasticity properties of wavelet transforms of speckled data, when these data are considered either with or without log-transform. The case where a log-transform is applied on multiplicative speckled data prior to wavelet transform is first associated with a framework of multiplicative (or geometric) wavelets. Then, through wavelet cumulant analysis, those multiplicative wavelets are shown to highlight both sparsity and stochasticity intrinsic to speckled data due to geometric differencing. In contrast, standard wavelet implementation (without log-transform) of speckled data yields intricate correlation structures which makes a clear separation between sparsity and stochasticity difficult, in particular for highly resolved data. The paper then derives that, for high resolution synthetic aperture radar data issued from airborne or new generation satellites, multiplicative wavelets represent a more relevant framework for the analysis of smooth earth fields observed in the presence of speckle. From this analysis, the paper derives a fast-and-concise multiplicative wavelet based method for joint change detection and regularization of synthetic aperture radar image time series. In this method, multiplicative wavelet details are first computed with respect to the temporal axis in order to derive change-images from the time series. The changes are then enhanced and speckle is attenuated by using sigmoid shrinkage functions. Finally, a regularized time series is reconstructed from the sigmoid shrunken change-images. An application to the analysis of RADARSAT-2 quad-polarimetric and SENTINEL-1A dual-polarimetric image time series over Chamonix-Mont-Blanc test site is proposed to show the relevancy and straightforwardness of the method.

Index Terms—Wavelets ; Geometric convolution ; Geometric approximations ; Geometric differencing ; Change detection, Regularization ; Synthetic Aperture Radar.

¹ LISTIC, EA 3703, Université Savoie Mont Blanc - Université Grenoble Alpes, France

² LTCI, CNRS UMR 5141, Telecom ParisTech, 46 rue Barrault, 75013 Paris, France

* Abdourrahmane.Atto@univ-smb.fr

The work was supported by the PHOENIX grant of the French national agency of research (ANR).

I. INTRODUCTION - MOTIVATION

HIGHLY resolved data such as Synthetic Aperture Radar (SAR) image time series issued from new generation sensors show minute details. Indeed, the evolution of SAR imaging systems is such that in less than 2 decades:

- high resolution sensors can achieve metric resolution, providing much richer spatial information than the decametric data issued from ERS or ENVISAT missions.
- the earth coverage has increased: recent satellites such as TerraSAR-X and Sentinel-1A have a dozen of days for repeating their cycle.

The increase of those spatial and temporal resolutions makes information extraction intricate in highly resolved SAR image time series. This compels us to re-consider data features and representations in order to simplify data storage and processing.

The paper presents a parsimonious framework on the analysis of huge data associated with multiplicative type interactions. These data are observed in many situations, for instance when acquiring signals from radar/sonar/ultrasonic waves [1]/[2]/[3],[4], when analyzing seasonality from meteorology data [5] or when focusing on proportionality in economy data [6] and political sciences [7]. From now on, we focus on SAR systems, a challenging imagery domain with huge amount of data affected by multiplicative type interaction.

From the literature, analysis of SAR image time series have been mainly performed on short-length image sequences. This is the consequence of SAR data cost (very high), long satellite revisit time and short satellite lifetime, among other issues. Literature concerns both theoretical and application guided methods for:

- identifying appropriate statistics/similarity measures [8], [9], [10], [11], [12], [13], [14], [15], [16], [17], *etc.*;
- detecting and analyzing specific features, for instance urban areas expansion [8], [18], [19], glaciers dynamics [13], [20], [21], snow cover mapping [22], sea clutter

analysis [23], forest mapping [24], earthquake monitoring [8], sea ice motion analysis [25], coastline detection [26], soil erosion [27], *etc.*;

- regularizing SAR data for speckle reduction and feature enhancement [19], [24], [26], [28], [29].

Most of these methods yield computationally complex algorithms because they have been built for the sole sake of performance over short-length image sequences.

For long-time sequences such as those expected with the future Sentinel constellation, a direct application of these methods is not an option: this direct application may be unthinkable due to computational cost and unnecessary for performance/robustness. Indeed, dense/long temporal sampling results in redundant information on the time axis so that a purely temporal analysis may be sufficient for monitoring of most large scale earth structures.

The issue raised by new generation SAR sensors is thus revisiting these methods with the sake of adapting them to long and dense temporal image samples. Among the references provided above, we consider hereafter wavelet based approaches derived in [8], [13] for change detection and in [29],[30] for image regularization.

For change detection, [8] computes a log-ratio change image and applies a wavelet transform to this log-ratio image in order to emphasize different levels of changes. In contrast, [13] computes the wavelet transform of images prior to change detection by using probabilistic pixel features.

For image regularization, [29] and [30] propose wavelet shrinkages by using a parametric Bayesian approach [29] and a non-parametric sigmoid based approach [30]. The wavelet transform applies on the spatial axes for both parametric and non-parametric methods, so as to be more robust to speckle. Despite the somewhat different strategy, parametric and non-parametric approaches can be shown equivalent up to a probabilistic prior specification.

The present paper revisit [8], [13], [29] and [30] for deriving a joint change detection and regularization framework. This framework assumes that several temporal observations of the pixel at stable states are available so that one can focus on the time axis for the wavelet transform (avoid a huge computational cost, suits for dense/long time series). This framework is based on generalized log-wavelet ratios so as to handle multiplicative type interactions.

A multiplicative observation model involving strictly positive interactions of a piecewise regular deterministic function f and a random process \mathbf{X} can be written as:

$$\mathbf{y} = f\mathbf{X} = f + f(\mathbf{X} - 1) \quad (1)$$

In the model given by Eq. (1), function f is observed in a multiplicative signal-independent-noise \mathbf{X} or, equivalently, in an additive signal-dependent-noise $f(\mathbf{X} - 1)$.

Given a transform \mathcal{W} for analyzing \mathbf{y} , the issue addressed in this paper is analyzing multiplicative and additive frameworks for the representation of \mathbf{y} . We assume that the properties desired for \mathcal{W} are both i) sparsity of representation of f and ii) simplification of the statistical properties of the noise involved in the model (stationarization and decorrelation properties, among others). In this respect, the transform \mathcal{W} will be associated to wavelet operators.

In the following, $\mathcal{W}\mathbf{y}$ refer to

- the (standard) additive wavelet transform, with (linearity with respect to ‘+’ operation):

$$\mathcal{W}\mathbf{y} = \mathcal{W}f + \mathcal{W}f(\mathbf{X} - 1), \quad (\clubsuit)$$

- the multiplicative (or *geometric*) wavelet transform, with (multiplicative linearity where \mathcal{W} distributes over ‘ \times ’ operation):

$$\mathcal{W}\mathbf{y} = (\mathcal{W}f) \times (\mathcal{W}\mathbf{X}). \quad (\spadesuit)$$

The term *geometric wavelet* is used because approximations based on multiplicative operations are referred to in the literature as *geometric statistics*: for instance, the mean statistics applying over ‘ \times ’ operators is known as the *geometric mean* [15].

Note that performing a geometric wavelet decomposition as presented in model (\spadesuit) amounts to apply a log-transform on the input data, perform a standard wavelet transform and apply an exponential transform on the wavelet coefficients of this standard transform. However, wavelet operators can be ‘embedded’ in a multiplicative algebra, so that their coefficients, called *geometric approximations* and *geometric differences*, involve specifically the \times operator used in (\spadesuit) . This embedding considers changing the algebra by using *binary internal multiplication* and *external power operation*. In this respect, this geometric approach contrasts significantly with ‘curvature’ based approaches (curvelets, bandlets, *etc.*, see [31] [32], [33], [34] for instance). Note that the same approach can be used to define geometric curvelets, bandlets, *etc.*, on multiplicative algebras.

The paper is organized as follows: Section II provides statistical properties of additive wavelet based transforms on model (\clubsuit) . The geometric wavelet inference is described in Section III. Its statistical properties (sparsity and stochasticity) on model (\spadesuit) are discussed in the same section. Section IV then exploits these statistical properties to provide a joint filtering and change detection of high resolution SAR image time series. Section V concludes the work. From now on, we assume that $\mathbf{X} = (\mathbf{X}[k])_{k \in \mathbb{Z}}$ denotes a stationary sequence of strictly positive real random variables.

II. WAVELET TRANSFORM AND MULTIPLICATIVE MODELS

A. Basics of wavelet based transforms

In the following, we are interested in multi-scale decomposition schemes involving paraunitary filters ($\mathbf{H}_0, \mathbf{H}_1$) associated with a wavelet decomposition, see [35], among other references.

A one-level wavelet decomposition involves splitting [36] a given functional space $\mathbf{W}_{j,n} \subset L^2(\mathbb{R})$, defined as the closure of the space spanned $\{\tau_{2^j k} W_{j,n} : k \in \mathbb{Z}\}$ into direct sums of subspaces $(\mathbf{W}_{j+1,2n+\epsilon})_{\epsilon \in \{0,1\}}$, spanned respectively by $\{\tau_{2^{j+1}k} W_{j+1,2n+\epsilon} : k \in \mathbb{Z}\}_{\epsilon \in \{0,1\}}$, where $\tau_k f : t \mapsto f(t-k)$. The splitting of $\mathbf{W}_{j,n}$ follows from decimated arithmetic convolution operations:

$$W_{j+1,2n+\epsilon}(t) = \sum_{\ell \in \mathbb{Z}} \mathbf{h}_\epsilon[\ell] W_{j,n}(t-2\ell). \quad (2)$$

for $\epsilon \in \{0,1\}$, where \mathbf{h}_ϵ denotes the impulse response of the *scaling filter* (when $\epsilon = 0$) or the *wavelet filter* (when $\epsilon = 1$).

The consequence of Eq. (2) is that a function g having coefficients $c = (c[\ell])_{\ell \in \mathbb{Z}} \in \ell^2(\mathbb{Z})$ on $\{\tau_{2^j k} W_{j,n} : k \in \mathbb{Z}\}$:

$$g = \sum_{\ell \in \mathbb{Z}} c[\ell] \tau_{2^j \ell} W_{j,n} \in \mathbf{W}_{j,n}$$

can be expanded¹ [35] in terms of

$$g = \underbrace{\sum_{\ell \in \mathbb{Z}} c_0[\ell] \tau_{2^{j+1} \ell} W_{j+1,2n}}_{\in \mathbf{W}_{j+1,2n}} + \underbrace{\sum_{\ell \in \mathbb{Z}} c_1[\ell] \tau_{2^{j+1} \ell} W_{j+1,2n+1}}_{\in \mathbf{W}_{j+1,2n+1}}$$

where its coefficients $c_\epsilon = (c_\epsilon[\ell])_{\ell \in \mathbb{Z}}$ on $\{\tau_{2^{j+1}k} W_{j+1,2n+\epsilon} : k \in \mathbb{Z}\}_{\epsilon \in \{0,1\}}$, for $\epsilon \in \{0,1\}$, where

$$c_\epsilon[k] = \sum_{\ell \in \mathbb{Z}} \mathbf{h}_\epsilon[\ell] c[\ell - 2k]. \quad (3)$$

Starting the decomposition from a function $f \in \mathbf{W}_{0,0}$,

$$f = \sum_{\ell \in \mathbb{Z}} c[\ell] \tau_\ell W_{0,0},$$

the subband $W_{j,n}$ coefficients of f follow from

$$c_{j,n}[k] = \sum_{\ell \in \mathbb{Z}} \mathbf{h}_{j,n}[\ell] c[\ell - 2^j k]. \quad (4)$$

where the Fourier transform $\mathbf{H}_{j,n}$ of $\mathbf{h}_{j,n}$ is (see [37, Eq. (26)]):

$$\mathbf{H}_{j,n}(\omega) = 2^{j/2} \left[\prod_{\ell=1}^j \mathbf{H}_{\epsilon_\ell}(2^{\ell-1} \omega) \right]. \quad (5)$$

Eq. (4) can be used in practice for computing discrete wavelet transforms from sample observations (terminologies of ‘discrete wavelet transform’ when $n \in \{0,1\}$, ‘discrete wavelet packet transform’ when $n \in \{0,1,\dots,2^j-1\}$,

¹Equalities hold in $L^2(\mathbb{R})$ sense in these expansions.

‘adapted discrete wavelet packets’ for a suitable selection of n -indices). Some splitting schemes involving non-decimation (factor 2^j in Eq. (4)) are also available and yield the concept of frames and the notion of stationary wavelet transforms [38]. The reader can refer to the abundant literature on wavelets for more details on wavelet transforms.

B. Additive wavelet transform and multiplicative observation model - Sparsity checking

Sparsity plays a major role for simplifying image storage and processing. For piecewise smooth signals, sparsity follows from the differencing operated by wavelet functions and the corresponding differences are called details (scaling functions operate as approximation functions).

SAR images are used hereafter for illustrating the behavior of additive/multiplicative wavelets on real data affected by multiplicative noise. For SAR imaging systems, interactions between coherent radar waves and ground surface result in the so-called *fully developed speckle* phenomenon, once the resolution cell (pixel) includes randomly distributed scatterers. The literature commonly assumes that SAR images are affected by a multiplicative (speckle) noise with unit mean and distributed - in amplitude as Rayleigh/exponential (single-look imaging) and Nakagami (multi-look imaging) - or - in intensity as Gamma (both single and multi look imaging). This literature also used to confirm that acquired data are not very sparse in the wavelet domain. In this respect, adaptive lifting wavelets [39] or redundant wavelet frames [40] are more often used for analysis purposes, in order to encompass this lack of strong sparsity.

Figures 1 and 2 present polarimetric SAR images acquired respectively by the DLR F-SAR and the RADASAT-2 sensors. Acquisitions have been performed by using coherent and polarized waves: Horizontal (H)/Vertical (V) for wave emission and Horizontal/Vertical for wave reception. Those polarimetric data are usually represented as a matrix of complex numbers composed of the 4 channels HH, HV, VH and VV. We have focused on the magnitudes of these complex data for image displays. The displays given by Figures 1 and 2 are color compositions where channels HH, HV and VV are associated with the colors blue, green and red respectively. These images illustrate multiplicative scattering phenomenon in the different polarimetric channels.

Figures 3 and 4 provide standard (additive) detail wavelet coefficients of polarimetric data given in Figures 1 and 2, respectively. The wavelet decomposition used is separable with respect to the different polarimetric channels and the Haar wavelet has been used for this decomposition.



Fig. 1. Polarimetric FSAR X-band image with size 5000×5000 pixels over Kaufbeuren site, Germany. The sensor used for this acquisition operates in the spectral X-band, has an altitude of 3045 meters and offers a pixel spacing of 15 centimeters in range and 17 centimeters in azimuth.

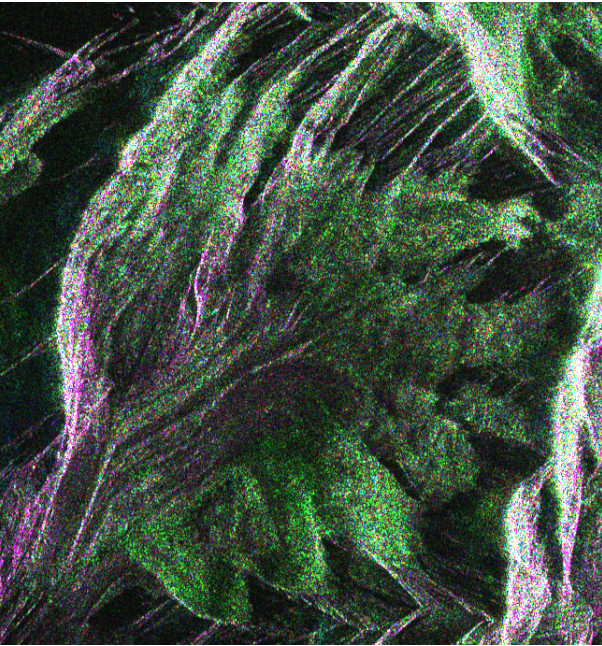


Fig. 2. Polarimetric RADARSAT-2 fine quad polarized image over the Talèfre glacier, Chamonix-Mont-Blanc test site, France.

In these detail coefficients, issued from additive wavelets on a multiplicative observation model, we observe many structures of the scene under consideration. In particular, we can even observe regular structures, which obviously might not be present in detail wavelet coefficients: regular structures are the domain of the scaling function and details must not contain varied regular structural infor-

mation in the case of strong sparsity.

Note that sparsity is a property applied on f . However, in a noisy environment, the useful sparsity is strongly linked to the noise properties since noise affects the non-zero coefficients, and thus affects the quality of the approximation that can be obtained by considering those non-zero coefficients. In order to explain this non-sparse behavior, the following addresses the properties of wavelet functions of the noise involved in (♣).

C. Stochasticity and the additive wavelet decomposition

In model (♣), the additive noise contribution is associated with a random sequence having the form

$$\mathbf{Y}[k] = f[k](\mathbf{X}[k] - 1). \quad (6)$$

Since we have assumed that $(\mathbf{X}[k])_{k \in \mathbb{Z}}$ are stationary with $\mathbb{E}\mathbf{X}[k] = \mu_0$ and autocorrelation function $R_{\mathbf{X}}[k, \ell] = \mathbb{E}[\mathbf{X}[k]\mathbf{X}[\ell]] \triangleq R_{\mathbf{X}}[k - \ell]$, then:

- The mean of $\mathbf{Y}[k]$ is

$$\mathbb{E}\mathbf{Y}[k] = f[k](\mu_0 - 1). \quad (7)$$

- The autocorrelation function of \mathbf{Y} , $R_{\mathbf{Y}}[k, \ell] = \mathbb{E}[\mathbf{Y}[k]\mathbf{Y}[\ell]]$ satisfies, by taking into account Eq. (6):

$$R_{\mathbf{Y}}[k, \ell] = f[k]f[\ell](R_{\mathbf{X}}[k - \ell] - 1). \quad (8)$$

Remark 1: Eqs. (7) and (8) above highlights that the additive signal-dependent noise \mathbf{Y} is non-stationary in general, except some few cases, for instance when f is constant.

Let us now analyze the wavelet coefficients of \mathbf{Y} . Denote by $C_{j,n}^+$ the coefficients of \mathbf{Y} on subband $\mathbf{W}_{j,n}$. We have

$$C_{j,n}^+[k] = \sum_{\ell \in \mathbb{Z}} \mathbf{h}_{j,n}[\ell] f[\ell - 2^j k] (\mathbf{X}[\ell - 2^j k] - 1). \quad (9)$$

It follows that

$$\mathbb{E}C_{j,n}^+[k] = (\mu_0 - 1) \sum_{\ell \in \mathbb{Z}} \mathbf{h}_{j,n}[\ell] f[\ell - 2^j k] \quad (10)$$

and the autocorrelation function $R_{j,n}^+[k, \ell] = \mathbb{E}[C_{j,n}^+[k]C_{j,n}^+[\ell]]$ of $C_{j,n}^+$ is:

$$R_{j,n}^+[k, \ell] = \sum_{p \in \mathbb{Z}} \sum_{q \in \mathbb{Z}} \mathbf{h}_{j,n}[p] \mathbf{h}_{j,n}[q] \times f[p - 2^j k] f[q - 2^j \ell] \times (R_{\mathbf{X}}[p - q - 2^j(k - \ell)] - 1) \quad (11)$$

From Eq. (11), we derive that $C_{j,n}^+$ is non-stationary in general due to the presence of the term $f[p - 2^j k] f[q - 2^j \ell]$ in Eq. (11) and this, even if $\mu_0 = 1$ in Eq. (10).

Remark 2 (Non-stationarity of $C_{j,n}^+$ for exponential type function f): Assume that $\mu_0 = 1$ and function f

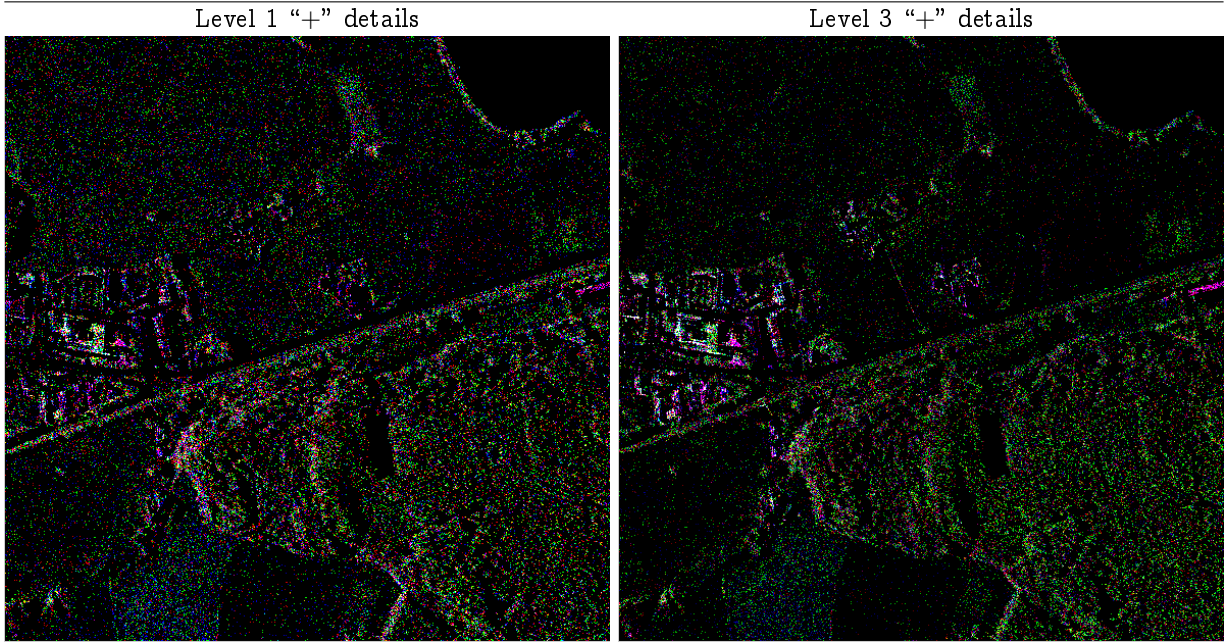


Fig. 3. Detail wavelet coefficients of the image given in Figure 1 when the Haar wavelet is used in an additive wavelet decomposition.

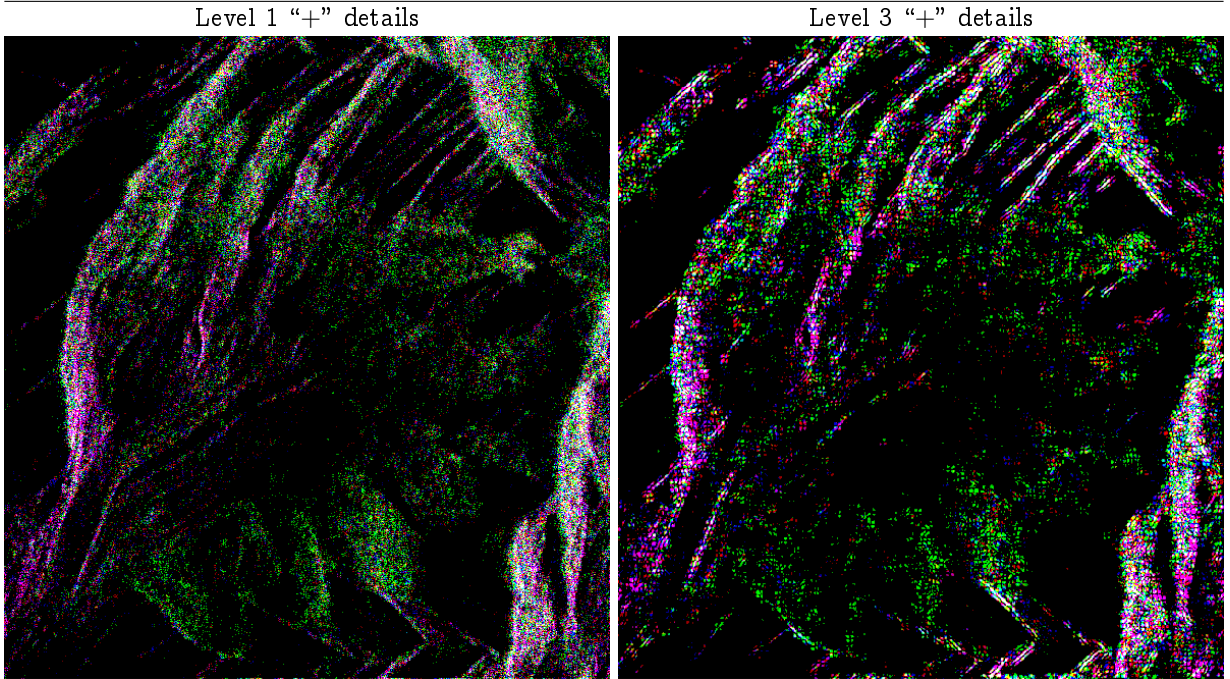


Fig. 4. Detail wavelet coefficients of the image given in Figure 2 when the Haar wavelet is used in an additive wavelet decomposition.

satisfies $f[k]f[\ell] = f[k + \ell]$ (exponential type functions), where f does not reduce to the constant 1. In this case, we derive

$$R_{j,n}^+[k,\ell] = \frac{f[-2^j(k+\ell)]}{2\pi} \int_{-\pi}^{\pi} \gamma_{\mathbf{x}^o}(\omega) |G_{j,n}(\omega)|^2 e^{i2^j(k-\ell)\omega} d\omega \quad (12)$$

where $G_{j,n} = F * \mathbf{H}_{j,n}$ and F is the Fourier transform of f . The non-stationarity of $C_{j,n}^+$ is then due to the term $f[-2^j(k+\ell)]$ in Eq. (12) above.

More generally, even when assuming that $\mu_0 = 1$, it is easy to check that most standard functions f lead to the non-stationarity of $C_{j,n}^+$. In particular, linear functions of type $f[k] = f_0 \times k$ (for certain k in a finite set) have a term in $k\ell$ which cannot be simplified in $R_{j,n}^+[k,\ell]$. High order polynomial functions have bivariate monomial terms involving $k^\lambda \ell^n$ in $R_{j,n}^+[k,\ell]$. Functions of type \sin, \cos satisfy $f[k]f[\ell] = g_1[k+\ell] + g_2[k-\ell]$ and in this case, the contribution of g_1 implies non-stationarity as in the exponential case given above, *etc.* From a practical

viewpoint, this non-stationarity is simply emphasized by Figures 3 and 4: in the areas where f is not constant, many f -structures (buildings)/ f -texture (forest, glacier) are present in detail wavelet coefficients.

An appealing case of stationarity sequence $C_{j,n}^+$ corresponds to a constant function f associated with a random sequence \mathbf{X} with unit mean:

Remark 3 (Stationarity): When $\mu_0 = 1$ and f is a constant function: $f[k] = f_0$, then $\mathbb{E}C_{j,n}^+[k] = 0$ and furthermore, we derive $R_{j,n}^+[k, \ell] = R_{j,n}^+[k - \ell] = R_{j,n}^+[m]$ with:

$$R_{j,n}^+[m] = \frac{f_0^2}{2\pi} \int_{-\pi}^{\pi} \gamma_{\mathbf{X}^0}(\omega) |\mathbf{H}_{j,n}(\omega)|^2 e^{i2^j m \omega} d\omega \quad (13)$$

where $\gamma_{\mathbf{X}^0}$ denotes the spectrum of the random sequence $\mathbf{X}^0 = \mathbf{X} - 1$.

$$\gamma_{\mathbf{X}^0}(\omega) = \sum_{m \in \mathbb{Z}} (R_{\mathbf{X}}[m] - 1) e^{-im\omega}.$$

This case of a constant function f observed in a multiplicative noise represents homogeneous area observation in practical SAR applications. This case is the sole favorable scenario for standard additive wavelets when the challenge is to simplify the multiplicative model $f\mathbf{X}$.

Due to the non-stationarity of $C_{j,n}^+$ in general (except few cases such as that of Remark 3), modeling or estimating additive wavelet coefficients of a multiplicative model is not an easy task. The following shows that multiplicative implementations of wavelets highlight desirable sparsity and stochasticity properties in model $f\mathbf{X}$.

III. EMBEDDING WAVELETS IN A MULTIPLICATIVE ALGEBRA

A. Geometric convolution

The binary operation considered in the following is the multiplication (\times symbol) over positive real numbers \mathbb{R}^+ (“0” has no sign and is not considered as a positive number).

Consider a data sequence $\mathbf{x} = (\mathbf{x}[\ell])_{\ell \in \mathbb{Z}}$, with $\mathbf{x}[\ell] \in \mathbb{R}^+$ for every $\ell \in \mathbb{Z}$. Since this sequence represents a multiplicative phenomenon, then

- “zero” or “nothing” or “no change” corresponds to the identity element “1”
- a “small” value is a value close to 1 (10^{-3} and 10^3 have the same significance in terms of *absolute proportion*,
- a missing value must be replaced by 1,
- shrinkage forces to 1, the coefficients that are close to 1.

The multiplicative algebra implies defining the support of the sequence \mathbf{x} as the sub-sequence composed with

elements that are different from 1. We will thus use the standard terminologies of finite/infinite supports with respect to the above remark. When such a sequence \mathbf{x} is infinite, we will assume that $\log(\mathbf{x}) = ((\log \mathbf{x}[k])_{k \in \mathbb{Z}}) \in \ell^2(\mathbb{Z})$.

When considering a scalar sequence (impulse response of a filter for instance) $\mathbf{h} = (\mathbf{h}[\ell])_{\ell \in \mathbb{Z}}$ where $\mathbf{h}[\ell] \in \mathbb{R}$ for every $\ell \in \mathbb{Z}$, then we will keep the standard terminology related to support definition from non-zero elements (non-null real numbers).

The geometric convolution defined below is based on this binary operation (notation $\mathbf{x} \times \mathbf{y} \triangleq \mathbf{x}\mathbf{y}$ for $\mathbf{x}, \mathbf{y} \in \mathbb{R}^+$) and real scalar power operations (notation $\mathbf{a} \wedge \mathbf{x} \triangleq \mathbf{x}^{\mathbf{a}}$ for $\mathbf{x} \in \mathbb{R}^+$ and $\mathbf{a} \in \mathbb{R}$).

Definition 1 (Geometric convolution): Let $\mathbf{h} = (\mathbf{h}[\ell])_{\ell \in \mathbb{Z}}$ denote the impulse response of a digital filter. We define the geometric convolution of \mathbf{x} and \mathbf{h} on the vector space $(\mathbb{R}^+, \times, \wedge)$ as:

$$\begin{aligned} \mathbf{y}[k] &= \mathbf{x} * \mathbf{h}[k] \triangleq \prod_{\ell \in \mathbb{Z}} (\mathbf{x}[\ell])^{\mathbf{h}[k-\ell]} \\ &= \prod_{\ell \in \mathbb{Z}} (\mathbf{x}[k-\ell])^{\mathbf{h}[\ell]} \triangleq \mathbf{h} * \mathbf{x}[k], \end{aligned} \quad (14)$$

One can remark that, in contrast to the standard convolution operation on the sequences of the field $(\mathbb{R}, +, \times)$, sequence \mathbf{h} plays a non-commutative scalar role with respect to \mathbf{x} since the external operation ‘power’ used in Eq. (14) is not commutative. This justifies the second \triangleq in Eq. (14): the equality $\mathbf{x} * \mathbf{h} = \mathbf{h} * \mathbf{x}$ applies index-wise on the geometric convolution, given that the scalar sequence \mathbf{h} operates to the power of elements of \mathbf{x} , by definition.

If $\mathbf{h} \in \ell^2(\mathbb{Z})$, then $\mathbf{x} * \mathbf{h}[k]$ exists and is finite for almost every k since we have assumed that $\log(\mathbf{x}) \in \ell^2(\mathbb{Z})$.

Depending on the filter \mathbf{h} used, Eq. (14) makes the computation of geometric approximations and differences of the input data \mathbf{x} possible. The standard geometric approximation (called *geometric mean*) of a finite sequence $\{\mathbf{x}_1, \mathbf{x}_2, \dots, \mathbf{x}_N\}$ is given by:

$$\mathbf{y} = \sqrt[N]{\mathbf{x}_1 \mathbf{x}_2 \cdots \mathbf{x}_N} = \prod_{\ell=1}^N \mathbf{x}_\ell^{1/N}. \quad (15)$$

This geometric mean (see Eq. (15)) is associated with an N -length Haar-like scaling filter

$$\mathbf{h}_0[k] = \mathbf{v} \text{ for } k = 1, 2, \dots, N. \quad (16)$$

Filter \mathbf{h}_0 (*low pass filter*) performs geometric approximations and can be associated with a Haar-like wavelet filter

$$\mathbf{h}_1[k] = (-1)^{k-1} \mathbf{v} \text{ for every } k = 1, 2, \dots, N. \quad (17)$$

which performs geometric differencing (*high pass* or *details*), where constant $\mathbf{v} > 0$ is fixed so as to impose paraunitarity for the corresponding pair of filters ($\mathbf{v} = \sqrt{2}/2$ for standard **Haar** wavelet filters when $N = 2$).

B. Geometric wavelet decomposition

In the following, we consider the same paraunitary wavelet filters $(\mathbf{h}_0, \mathbf{h}_1) \in \ell^2(\mathbb{Z}) \times \ell^2(\mathbb{Z})$ as in Section II. Let

$$\overline{\mathbf{h}[k]} = \mathbf{h}[-k].$$

Define the wavelet decomposition of \mathbf{x} with respect to the geometric convolution (*geometric wavelet decomposition*) by:

$$\mathbf{c}_{1,0}[k] = \mathbf{x} * \overline{\mathbf{h}_0}[2k], \quad (18)$$

$$\mathbf{c}_{1,1}[k] = \mathbf{x} * \overline{\mathbf{h}_1}[2k], \quad (19)$$

and, recursively, for $\epsilon \in \{0, 1\}$ (wavelet packet splitting formalism described in [36]):

$$\mathbf{c}_{j+1,2n+\epsilon}[k] = \mathbf{c}_{j,n} * \overline{\mathbf{h}_\epsilon}[2k]. \quad (20)$$

In the decomposition given by Eq. (20) above, sequence $\mathbf{c}_{j+1,2n+\epsilon}$ represents:

- geometric approximations of $\mathbf{c}_{j,n}$ when $\epsilon = 0$,
- geometric differences (details) of $\mathbf{c}_{j,n}$ when $\epsilon = 1$.

The level $j = 0$ coefficients represent the input sequence \mathbf{x} . The above wavelet packet splitting is associated to a wavelet decomposition when the splitting concerns only $(\mathbf{c}_{j,0})_{j \geq 1}$

Proposition 1 (*Geometric wavelet reconstruction*):

We have:

$$\mathbf{c}_{j,n}[k] = (\check{\mathbf{c}}_{j+1,2n} * \mathbf{h}_0[k]) \times (\check{\mathbf{c}}_{j+1,2n+1} * \mathbf{h}_1[k]). \quad (21)$$

where

$$\check{\mathbf{u}}[2k + \epsilon] = \begin{cases} \mathbf{u}[k] & \text{if } \epsilon = 0, \\ 1 & \text{if } \epsilon = 1. \end{cases} \quad (22)$$

Proof: The proof is a direct consequence of the expansion of the right hand side of Eq. (21), by taking into account Eq. (20) and the paraunitary condition which imposes $\sum_{\ell \in \mathbb{Z}} \mathbf{h}_\epsilon[\ell] \overline{\mathbf{h}_\epsilon}[\ell - 2k] = \delta[k]$. ■

Proposition 1 represents the reconstruction of the level- j -wavelet-coefficients from the coefficients located at level $j + 1$. As in the standard additive formulation given in Section II (see Eq. (3)), different wavelet decomposition schemes (orthogonal wavelets, stationary wavelets, adapted wavelet packets, *etc.*) and perfect reconstructions can be obtained from Eqs. (20) and (21) respectively.

This geometric transform is the formalization of different operations performed by SAR community in processing SAR images. Indeed, its implementation derives from from standard additive wavelet transform since it consists in:

- replacing the standard convolution by the geometric convolution given in Definition 1 and,
- noticing that decimation corresponds to replacing one coefficient out of two by the number 1.

This implementation is exactly what one gets with standard wavelet transform by using log transform before transforming data and exp transform after data transforming. In the following, we will address the statistical properties of the coefficients issued from Eq. (20).

C. Multiplicative wavelet transform and multiplicative observation model - Sparsity checking

Section II-B has emphasized the lack of sparsity of the additive wavelet details when dealing with a multiplicative observation model (see Figures 3 and 4 for instance). In order to seek sparse detail representations for the multiplicative model, changing wavelet functions by considering other types of functional bases is not necessary: we just need to apply a convolution operation adapted to our sampling process. Indeed, since a given natural scene (such as those involved in Figures 1, 2) can be coarsely described as a piecewise smooth function, then wavelets are expected to capture the intrinsic redundancy of such a scene in a sparse way, independently of the intrinsic properties of the acquisition device.

For the SAR images, this operation is described by a multiplicative type interaction between signal and speckle noise. In this respect, wavelet based decompositions should also be multiplicative for sparsity to holds true in the wavelet detail domain.

Figures 5 and 6 provide geometric (multiplicative) detail wavelet coefficients of polarimetric images given by Figures 1 and 2 respectively. When analyzing these detail coefficients, we observe only very few structures of the noise-free signal. Multiplicative wavelet details are thus more convenient for sparse based analysis than additive wavelet coefficients for this observation model. Note that for the multiplicative model (♠), sparsity denotes a large number of ‘ones’ and detail wavelet images of Figures 5 and 6 have been displayed in a logarithmic scale so as to make comparison with Figures 3 - 4 possible.

D. Stochasticity and the geometric wavelet decomposition

In model (♠), noise contribution is multiplicative and associated with a unit-mean stationary random sequence $\mathbf{X} = (\mathbf{X}[k])_{k \in \mathbb{Z}}$. Note that the geometric wavelet decomposition of Eq. (20), say \mathcal{W}^\times , distributes over the product $f\mathbf{X}$: $\mathcal{W}^\times[f\mathbf{X}] = (\mathcal{W}^\times f)(\mathcal{W}^\times \mathbf{X})$. In this respect, the focus of this Section are the statistical properties of $\mathcal{W}^\times \mathbf{X}$. The subband $\mathbf{W}_{j,n}$ geometric wavelet coefficients of the decomposition of \mathbf{X} will be denoted $(\mathbf{C}_{j,n}^\times)_{j,n}$ (we assume that this stochastic sequence is well defined in the following).

Note that if $\mathbf{C}_{j+1,2n+\epsilon}[k] = \mathbf{C}_{j,n} * \overline{\mathbf{h}_\epsilon}[2k]$ where $\mathbf{C}_{j,n}$ is a stationary sequence, then $\mathbf{C}_{j+1,2n+\epsilon}$ is also stationary. Since $\mathbf{C}_{0,0} = \mathbf{X}$ is assumed to be stationary, we derive

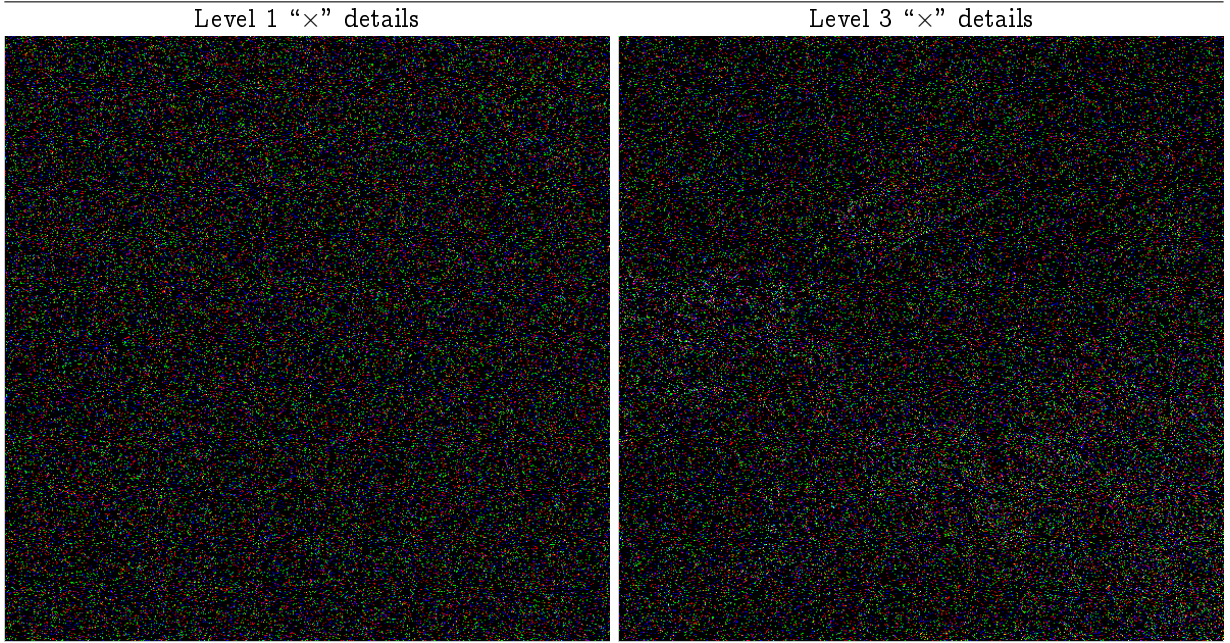


Fig. 5. Diagonal detail wavelet coefficients of the image given in Figure 1 when the Haar wavelet is used in a multiplicative wavelet decomposition.

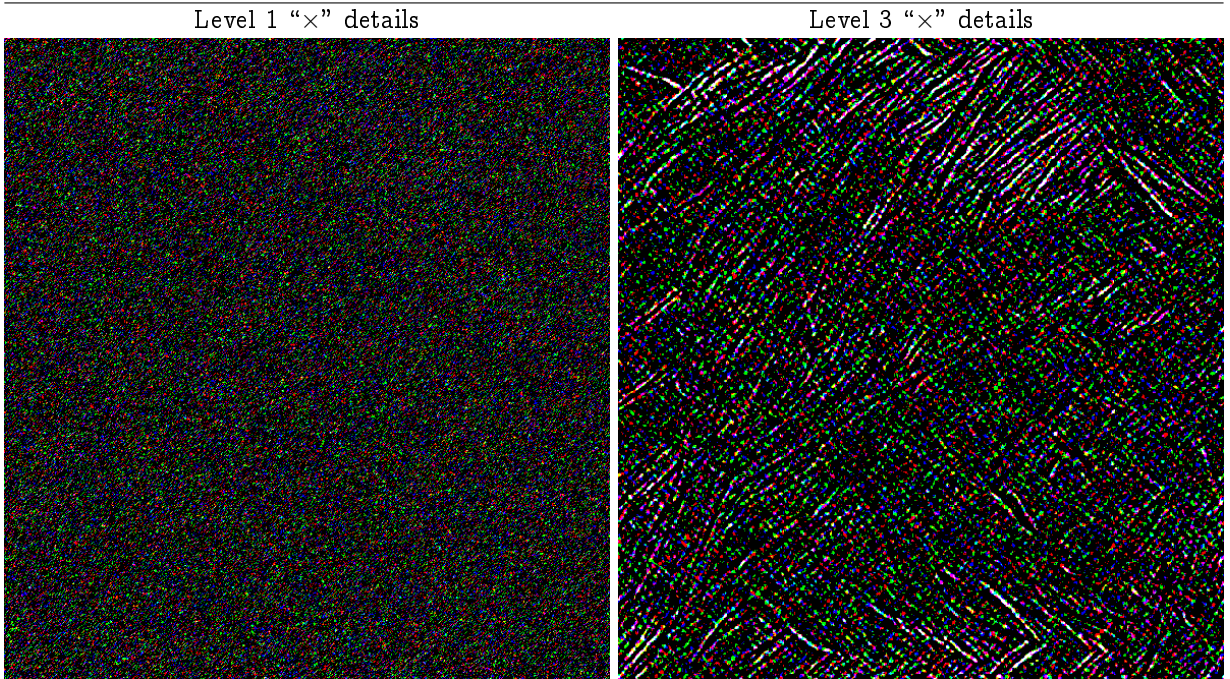


Fig. 6. Diagonal detail wavelet coefficients of the image given in Figure 2 when the Haar wavelet is used in a multiplicative wavelet decomposition.

that all geometric wavelet sequences $\mathbf{C}_{j,n}$ are stationary for $j \geq 0$ and $n \in \{0, 1, \dots, 2^j - 1\}$.

Let $\mathbf{Y} = \log \mathbf{X}$. We assume hereafter that \mathbf{Y} is a second-order random process, continuous in quadratic mean. Let $\mathbf{D}_{j,n} = \log \mathbf{C}_{j,n}^\times$. Note that \mathbf{Y} and $\mathbf{D}_{j,n}$ are stationary sequences. Assume that $\mathbb{E}\mathbf{Y}[k] = 0$ for every $k \in \mathbb{Z}$. Then $\mathbb{E}\mathbf{D}_{j,n}[k] = 0$ for every $k \in \mathbb{Z}$.

Let $R_{\mathbf{Y}}[m] = R_{\mathbf{Y}}[k-\ell] = \mathbb{E}[\mathbf{Y}[k]\mathbf{Y}[\ell]]$ be the autocorre-

lation function of \mathbf{Y} , where the first equality above holds true for any pair $(k, \ell) \in \mathbb{Z} \times \mathbb{Z}$ such that $m = \pm|k - \ell|$. Proposition 2 below derives the autocorrelation function $R_{\mathbf{D}_{j,n}}$ of the log-scaled geometric wavelet coefficient $\mathbf{D}_{j,n}$. We assume that $\sum_{q \in \mathbb{Z}} \mathbf{h}_\epsilon[p - 2k]\mathbf{h}_\epsilon[q - 2\ell]R_{\mathbf{D}_{j,n}}[p, q]$ exists for every $j \geq 0$ and $n \in \{0, 1, \dots, 2^j - 1\}$.

Proposition 2 (Autocorrelation Function of $\mathbf{D}_{j,n}$):

Assume that R_Y has a spectrum (power spectral density)

$$\gamma_Y(\omega) = \sum_{m \in \mathbb{Z}} R_Y[m] e^{-im\omega}$$

and that γ_Y is bounded. Denote by $\gamma_{D_{j,n}}$, the spectrum of $D_{j,n}$:

$$\gamma_{D_{j,n}}(\omega) = \sum_{m \in \mathbb{Z}} R_{D_{j,n}}[m] e^{-im\omega} \quad (23)$$

We have, for $j \geq 0$, $n \in \{0, 1, \dots, 2^j - 1\}$ and $\epsilon \in \{0, 1\}$:

$$R_{D_{j+1, 2n+\epsilon}}[m] = \frac{1}{2\pi} \int_{-\pi}^{\pi} |\widehat{H}_{\epsilon}(\omega)|^2 \gamma_{D_{j,n}}(\omega) e^{2im\omega} d\omega \quad (24)$$

where $\gamma_{D_{0,0}} = \gamma_Y$.

Proof: See Appendix A. ■

By taking into account that sequence $D_{j,n}$ issues from a filter bank $(H_{\epsilon_\ell})_{\ell=1,2,\dots,j}$ (low-pass when $\epsilon_\ell = 0$ and high-pass when $\epsilon_\ell = 1$) and has the equivalent representation given by Eq. (5), we derive recursively from Eq. (24):

$$R_{D_{j,n}}[m] = \frac{1}{2\pi} \int_{-\pi}^{\pi} |\mathbf{H}_{j,n}(\omega)|^2 \gamma_Y(\omega) e^{2im\omega} d\omega \quad (25)$$

Eq. (25) governs the behavior of the autocorrelation of $D_{j,n}$. From this equation, decorrelating geometric wavelet coefficients involves selecting wavelet filters such that

$$\frac{1}{2\pi} \int_{-\pi}^{\pi} |\mathbf{H}_{j,n}(\omega)|^2 \gamma_Y(\omega) \cos 2^j m \omega d\omega \quad (26)$$

behaves approximately as $\delta[m]$. This is strongly linked to the shape of γ_Y and can be achieved by

- (i) choosing a sequence of wavelet filters such that function $|\mathbf{H}_{j,n}(\omega)|^2 \gamma_Y(\omega)$ can be seen as approximately constant or
- (ii) seek asymptotic decorrelation with j , when it applies.

Item (i) is parametric in the sense that it relates to adapted wavelet selection for decorrelating Y . Item (ii) (non-parametric) exploits properties of recursive convolutions. For instance, if we consider the Haar wavelet filters (used below for illustrations), we can derive :

Proposition 3 (*Haar equivalent wavelet filter sequence $\mathbf{H}_{j,n}^{Haar}$*): A sequence $(\mathbf{h}_{\epsilon_\ell})_{\ell=1,2,\dots,j}$ has equivalent filter:

$$|\mathbf{H}_{j,n}^{Haar}(\omega)|^2 = 2^j \prod_{\ell=1}^j \cos^2 \left(2^{\ell-2} \omega + \epsilon_\ell \frac{\pi}{2} \right). \quad (27)$$

Proof: See Appendix B. ■

In the usual wavelet splitting scheme, only approximation coefficients are decomposed again (the shift parameter $n \in \{0, 1\}$). This implies filtering sequences with the form

$$\left(\underbrace{\mathbf{h}_0, \mathbf{h}_0, \dots, \mathbf{h}_0}_{j \text{ times}}, \mathbf{h}_{\epsilon_{j+1}} \right)_{\epsilon_{j+1} \in \{0,1\}}$$

at decomposition level $j+1$. Consider a j -length approximation sequence $(\mathbf{h}_0^{Haar})_{\ell=1,2,\dots,j}$ of Haar type. Then from Eq. (27), the equivalent filter of this sequence can be rewritten in the form:

$$|\mathbf{H}_{j,0}^{Haar}(\omega)|^2 = 2^j \left(\frac{\text{sinc}(2^{j-1}\omega)}{\text{sinc}(2^{-1}\omega)} \right)^2 \quad (28)$$

where sinc denotes the *cardinal sine* function, $\text{sinc}\omega = \sin\omega/\omega$. The autocorrelation $R_{D_{j,0}}^{Haar}$ of the corresponding geometric wavelet coefficients is then:

$$R_{D_{j,0}}^{Haar}[m] = \frac{2^j}{\pi} \int_0^\pi \left(\frac{\text{sinc}(2^{j-1}\omega)}{\text{sinc}(2^{-1}\omega)} \right)^2 \gamma_Y(\omega) \cos 2^j m \omega d\omega \quad (29)$$

Proposition 4 (*Limit Autocorrelation Function*):

$$\lim_{j \rightarrow +\infty} R_{D_{j,0}}^{Haar}[m] = \gamma_Y(0) \delta[m] \quad (30)$$

Proof: See Appendix C. ■

Proposition 4 highlights an asymptotic decorrelation property with j . This property can be extended by considering different paraunitary filters. For instance, when considering the N -length Haar type paraunitary approximation filter \mathbf{h}_0 and detail filter \mathbf{h}_1 given by Eqs. (16) and (17), the equivalent wavelet filter is

$$|\mathbf{H}_{j,n}(\omega)|^2 = 2^j \prod_{\ell=1}^j \left(\frac{\sin(2^{\ell-2} N \omega)}{\sin(2^{-1}(\omega + \epsilon_\ell \pi))} \right)^2 \quad (31)$$

It follows that the corresponding autocorrelation $R_{D_{j,n}}$ is

$$\begin{aligned} R_{D_{j,n}}[m] &= \frac{2^j}{\pi} \int_0^\pi \prod_{\ell=1}^j \left(\frac{\sin(2^{\ell-2} N \omega)}{\sin(2^{-1}(\omega + \epsilon_\ell \pi))} \right)^2 \gamma_Y(\omega) \cos 2^j m \omega d\omega, \\ &= \frac{1}{\pi} \int_0^\pi \prod_{\ell=1}^j \left(\frac{\sin(2^{-j+\ell-2} N \omega)}{\sin(2^{-j-1}(\omega + \epsilon_\ell \frac{\pi}{2}))} \right)^2 \gamma_Y \left(\frac{\omega}{2^j} \right) \cos m \omega d\omega \end{aligned}$$

which tends to $\gamma_Y(0) \delta[m]$ when j tends to infinity, for the approximation path ($n=0$).

This decorrelation property can also be extended by considering different paths, filters and wavelet packet splitting schemes, as done in [37] for additive noise and arithmetic wavelet transforms.

From the stationarity and decorrelation properties shown in this section, it follows that Model (♠) is suitable for statistical analysis of observation $f\mathbf{X}$ since multiplicative wavelet coefficients define a stationary sequence $\mathbf{C}_{j,n}^\times$ (validation of the stationary behavior observed in Figures 5 - 6) and the form of the autocorrelation of this sequence can be specified for decorrelation purposes through a selection of adapted filter $\mathbf{H}_{j,n}$ in Eq. (25).

In the rest of the paper, we consider the multiplicative wavelet transform for and easy detection of changes on the time axis (sparsity of the temporal details) and a joint change detection + regularization framework.

IV. MULTIPLICATIVE WAVELETS FOR JOINT CHANGE DETECTION AND REGULARIZATION OF SAR IMAGE TIME SERIES

A. Principle for joint change detection and regularization

We consider a PolSAR scattering/covariance image time series $\mathcal{C} = (\mathcal{C}_{m,n}^{uv}(k))$, where $(u, v) \in \{H, V\} \times \{H, V\}$, H/V stands for *Horizontal / Vertical* respectively, (m, n) refers to spatial domain and k denotes time axis. We have $\mathcal{C}_{m,n}^{uv}(k) = \mathcal{I}_{m,n}^{uv}(k) \Theta_{m,n}^{uv}(k)$ where \mathcal{I} denotes moduli and Θ stands for unit-norm complex exponential phase terms. The temporal multiplicative wavelet transform is chosen to apply on $\mathcal{I}_{m,n}^{uv}(\bullet)$: the transform is performed to decompose series $\mathcal{I}_{m,n}^{uv}(k)$ with respect to the time variable k solely. Terms $\Theta_{m,n}^{uv}(k)$ are stored and added after processing of \mathcal{I} .

The spatio-temporal multiscale wavelet change information is concentrated in multiplicative detail subbands hereafter called *change-images*. The change analysis involves using a spatio-temporal block shrinkage for the retrieval of multi-temporal multi-scale multiplicative wavelet coefficients associated with change information. The shrunken multiplicative wavelet change-images are then used to reconstruct a regularized time series with sharp change transitions. The shrinkage thus makes both retrieval of temporal changes and obtaining a regularized image time series possible.

The shrinkage addressed below will apply through *sigmoid shrinkage* functions [30]. These functions have the following form:

$$\delta_{t,\theta,\lambda}(x) = \frac{\text{sgn}(x)(|x| - t)_+}{\left(1 + e^{-\zeta(\theta)\left(\frac{|x|}{\lambda} - 1\right)}\right)} \quad (32)$$

where

$$\zeta(\theta) = \frac{10 \sin \theta}{2 \cos \theta - \sin \theta} \quad (33)$$

and $\text{sgn}(x) = 1$ (resp. -1) if $x \geq 0$ (resp. $x < 0$), and $(x)_+ = x$ (resp. 0) if $x \geq 0$ (resp. $x < 0$).

Note that since the wavelet transform is performed with respect to the time axis, a wavelet based change image (temporal detail image) contains:

- either a bidate change information (level $j = 1$ detail coefficients when using a filter \mathbf{h} with 2 non-zero coefficients, such as Haar filters)
- or a multirate change information when:
 - $j \geq 2$, whatever the filter used, provided that the filter has at least 2 non-zero coefficients,
 - $j \geq 1$, when the filter used has more than 2 non-zero coefficients.

For highlighting the multitemporal changes in their spatio-temporal context, the above sigmoid shrinkage function will be applied hereafter in a spatio-temporal framework (spatial blocks on wavelet based temporally differenced

data). For a pixel moduli $Z_{m,n}^{uv}(k)$ pertaining to a log-scaled change-image, the shrinkage proposed is defined as:

$$\delta_{t,\theta,\lambda}(Z_{m,n}^{uv}(k)) = \frac{\text{sgn}(Z_{m,n}^{uv}(k))(|Z_{m,n}^{uv}(k)| - t)_+}{1 + e^{-\zeta(\theta)\left(\frac{\|V_{Z_{m,n}^{uv}(k)}\|_2}{\lambda} - 1\right)}} \quad (34)$$

where $V_{Z_{m,n}^{uv}(k)}$ is a vector with the form $V_{Z_{m,n}^{uv}(k)} = \{Z_{m,n}^{uv}(k), \mathbf{m} = \mathbf{m} - \epsilon_0, \dots, \mathbf{m} + \epsilon_0, \mathbf{n} = \mathbf{n} - \nu_0, \dots, \mathbf{n} + \nu_0\}$ and ϵ_0, ν_0 are natural numbers chosen sufficiently small (spatial neighborhood of the detail pixel $(Z_{m,n}^{uv}(k))$, with $\|\cdot\|_2$ denoting the ℓ^2 norm. This penalized shrinkage then consists in

- forcing to zero all temporal log-scaled geometric wavelet change-image pixel with spatial neighborhood norm smaller than the first threshold t ,
- attenuating temporal log-scaled geometric wavelet change-image pixel with large spatial neighborhood norm thanks to an attenuation degree θ and a second threshold λ .

Note that when 2^J PolSAR image samples are available, then, by restricting the wavelet transform to apply on the time axis and by performing a level J decomposition, we have to take into account:

- the level J subband of this sequence, which reduces to a single PolSAR image called hereafter PolSAR geometric *approximation image* or *mean-image*,
- the levels $j = 1, 2, \dots, J$ change-images, with 2^{J-j} change-images at decomposition level $j \leq J$ (decimation in order to reject redundant change information).

B. Application to RADARSAT-2 quad-polarimetric SAR image time series (short sequence)

The test site considered in this example is an area covering the glaciers *Mer de Glace* and *Argentière*, in the mountainous Chamonix-Mont-Blanc site, in France. Figure 7-left presents a 4-length SAR image time series denoted \mathcal{P} of this test site (RADARSAT-2 satellite fine quad polarization). The scene displayed (50 km² approximately) is an RGB color composition from polarimetric scattering vectors.

The geometric wavelet coefficients of \mathcal{P} are given in Figure 7-right. Since $J = 2$ (\mathcal{P} is a $4 = 2^J$ -length PolSAR image time series) for this example, we have 3 multiscale change-images for an orthogonal geometric wavelet decomposition scheme (2 change-images at the first scale and 1 change-image at the second scale). In addition, because we have considered the Haar wavelets, then:

- level-1 change-images (finer details) are geometric differences (ratios) between consecutive acquisitions ($\mathcal{P}(k)$ versus $\mathcal{P}(k-1)$), in addition with a decimation step (case of the orthogonal decimated wavelet transform),

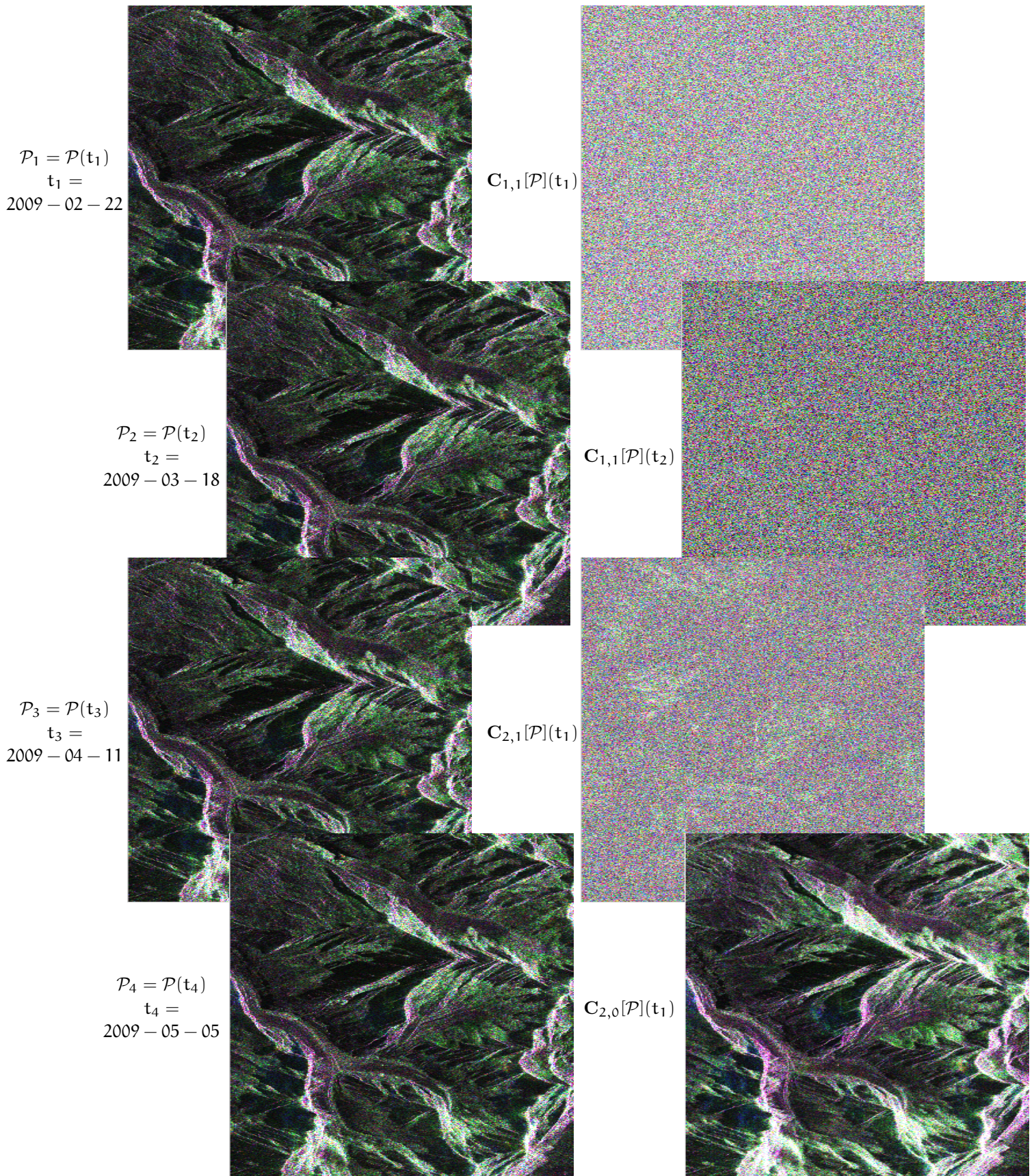


Fig. 7. Left: RADARSAT-2 quad PolSAR image time series over 2 glaciers (*Mer de Glace* and *Argentière*) of the Mont-Blanc mountain. Right: geometric wavelet coefficients of this image time series by using Haar wavelets.

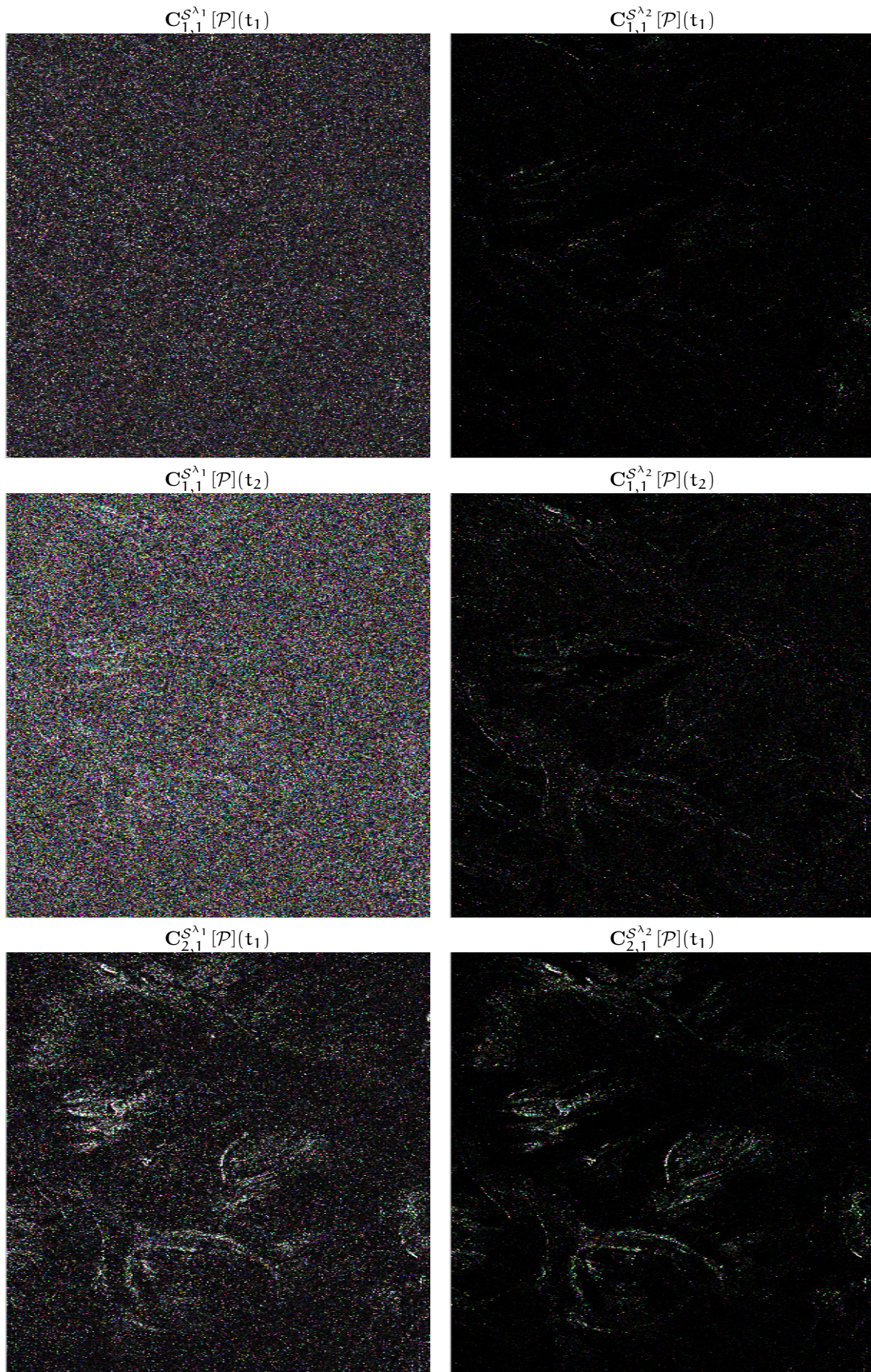


Fig. 8. Sigmoid shrinkage with $\lambda = \lambda_1$ (left) and $\lambda = \lambda_2$ (right) of the detail coefficients given in Figure 7. Images provide multilevel change maps.

- level-2 coefficients provide coarser change-images in terms of ratios ($\mathcal{P}(k), \mathcal{P}(k-1)$ versus $\mathcal{P}(k-2), \mathcal{P}(k-3)$) (4 dates involved in the two pairs).

The geometric change-images given in Figure 7-right show both sparsity of change information (changes are rare and significant when present) and stationarity in homogeneous areas with no temporal change (speckle noise). These results are consequences of the multiplicative wavelet transform accuracy for a sparse+stochastic representation of a multiplicative observation model (see Sections II and III).

The multitemporal change information present in these geometric change-images can thus be highlighted and detected with high performance by using shrinkage functions in the geometric wavelet domain.

We then apply the block sigmoid shrinkage given by Eq. (34) to the change-images of Figure 7-right with parameters t_0 chosen as the universal threshold of [41], $\theta = \pi/5$ and $\lambda \in \{\lambda_1, \lambda_2\}$, where $\lambda_1 = t_0$, $\lambda_2 = 2t_0$. This sigmoid shrinkage, denoted by an operator S^λ yields change-images of Figure 8.

As it can be seen in Figure 8, shrinkage S^{λ_1} highlights many small change structures (compare details of Figure 7-right with those of Figure 8-left) and the detection is made highly selective by using S^{λ_2} (compare Figure 8-right with Figures 7-right and 8-left).

C. Application to Sentinel-1A dual-polarimetric SAR image time series

The geometric temporal wavelet shrinkage for both change detection and regularization aims at simplifying the analysis of long time series of SAR images. Indeed, the challenge in exploiting such huge data is in dimensionality handling and requires methods that have very low computational load.

Sentinel constellation of the European Space Agency (ESA) is a source of highly resolved spatio-temporal data. Since the launch of Sentinel-1A in April 2014, a time series of PolSAR data over the Chamonix-Mont-Blanc test site has been collected and co-registered thanks to a fixed corner reflector, see Figure 9 (images are available free of charge from ESA repository). This time series is composed of 11 dual PolSAR IW level-1 Single Look Complex (SLC) SAR images acquired in descending pass from November 15, 2014 to March 15, 2015 with 12 days sampling period. The resolution is about 3.5×20 squared meters for SLC images. Images are here displayed in a Pauli color rendering in order to enhance dual-polarimetry information.

Different types of changes can occur on this glacier site due to the long period of observation: for instance snow fall, snow accumulation in specific areas, serac falls,

avalanches, human activities, *etc.* It is worth noticing that a pixel-per-pixel and date-per-date search is possible, see for instance [42]. However, this is with very high computational cost, in comparison with the geometric temporal wavelet shrinkage proposed below. Specifically, we consider both scalar sigmoid shrinkage (polarimetry channels are considered independently for building V_Z in Eq. (34)) and vector sigmoid shrinkage (V_Z is a sequence of ℓ_p -norms of PolSAR channels) for comparison purpose. If we assume that parameter t of sigmoid shrinkage equals 0 (no zero forcing), then the shrinkage of PolSAR vector coefficient $Z_{m,n}(k) = (Z_{m,n}^{uv}(k))_{(u,v) \in (H,V)^2}$ reduces to

$$\delta_{t,\theta,\lambda}(Z_{m,n}(k)) = \frac{Z_{m,n}(k)}{1 + e^{-\zeta(\theta) \left(\frac{\|V_{||Z_{m,n}(k)||_p}\|_2}{\lambda} - 1 \right)}} \quad (35)$$

where $\zeta(\theta)$ is given by Eq. (33) and V is constructed as done in Section IV-A.

Some geometric wavelet change-images are given by Figure 10 (we restrict to level $j = 2$ temporal changes due to the limited size of the paper). As expected, these details looks stochastic, excepted in few areas. Scalar sigmoid shrinkage (polarimetry channels are considered independently) yields change-images of Figure 11 whereas vector sigmoid shrinkage leads to change-images of Figure 12. One can notice that the latter better enhances polarimetry change information than the former. An analysis of the areas affected by changes highlights that these are urban areas and the Argentière glacier serac fall area. In addition to changes in these dynamic areas, one can note some specific very localized changes, for instance the one near Argentière glacier accumulation area (see Figure 13 for localizing the most important changes and the corresponding areas). The borders of *Mer de glace* glacier also tend to yield change responses both in RADARSAT-2 data (see Figure 8) and in Sentinel-1 data (see Figure 12). This can be due to co-registration errors. However, since Argentière glacier borders do not respond equivalently, this suspect behavior needs to be confront with ground truth because these change responses can reveal other phenomena such as glacier constriction.

By applying inverse geometric wavelet transform on shrunken change-images, we derive regularized time series given by Figures 14 (scalar sigmoid case) and 15 (vector polarimetry case). The comparison with Figures 9, 14 and 15 emphasizes nice properties in both regularization and change preservation for the vector sigmoid geometric wavelet shrinkage.

V. CONCLUSION

This paper has derived statistical properties of wavelets in additive and multiplicative implementation frameworks. Multiplicative wavelets are explained in terms of

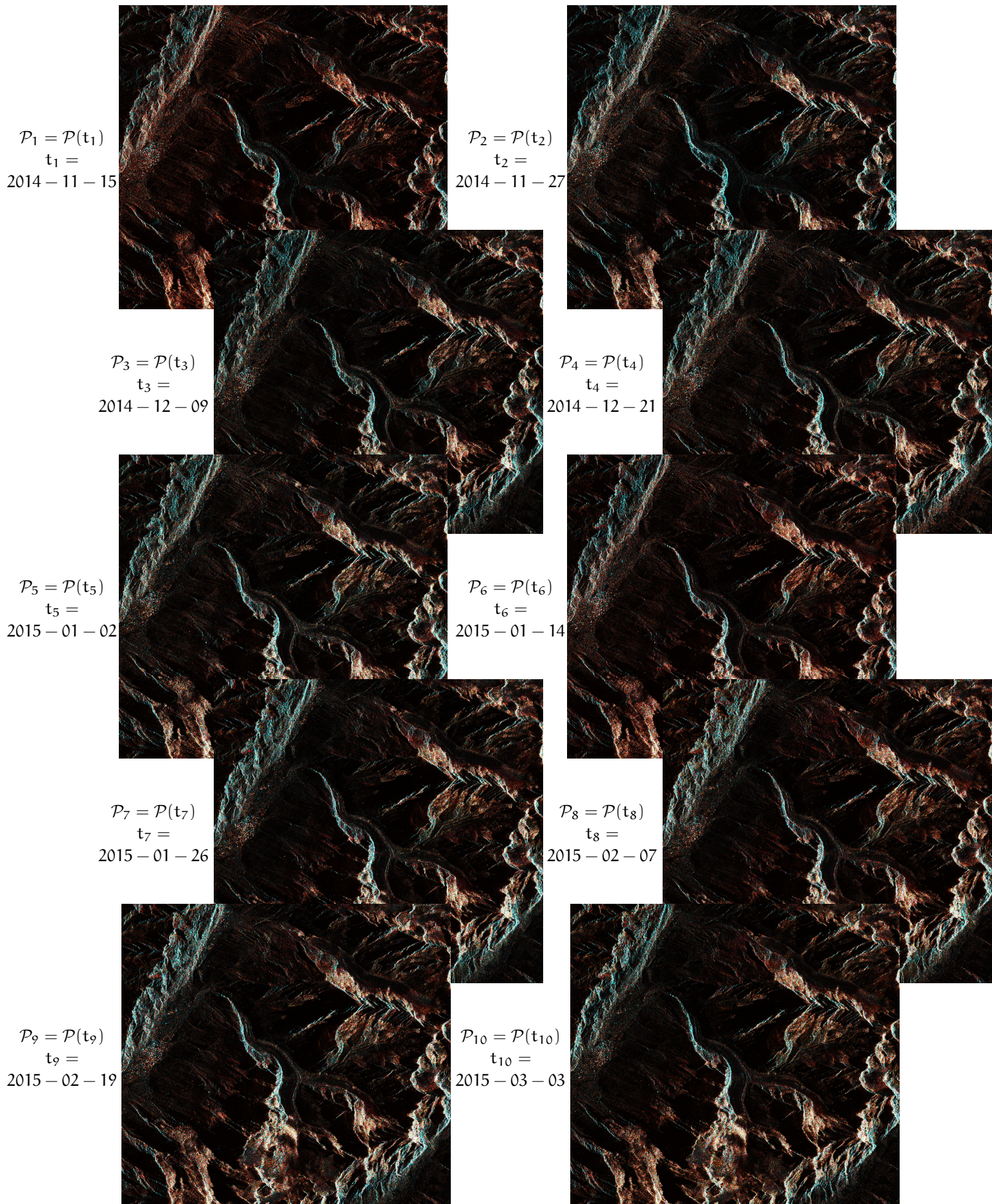


Fig. 9. Sentinel-1A dual PolSAR image time series \mathcal{P} over 2 glaciers (*Mer de Glace* and *Argentière*) of the Mont-Blanc mountain.

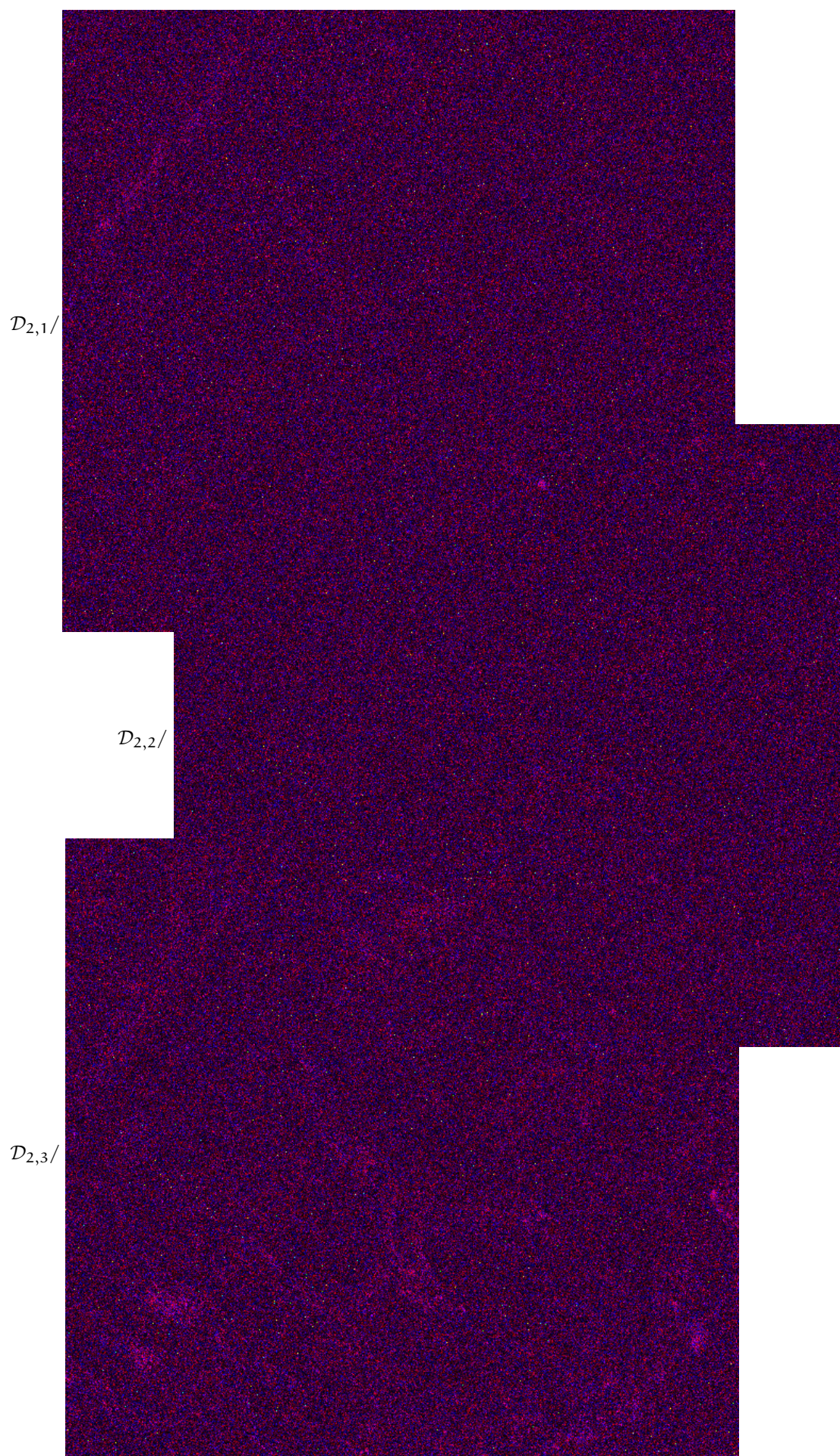


Fig. 10. Level 2 geometric wavelet change-images of the Sentinel-1A dual PolSAR image time series \mathcal{P} of Figure 9.

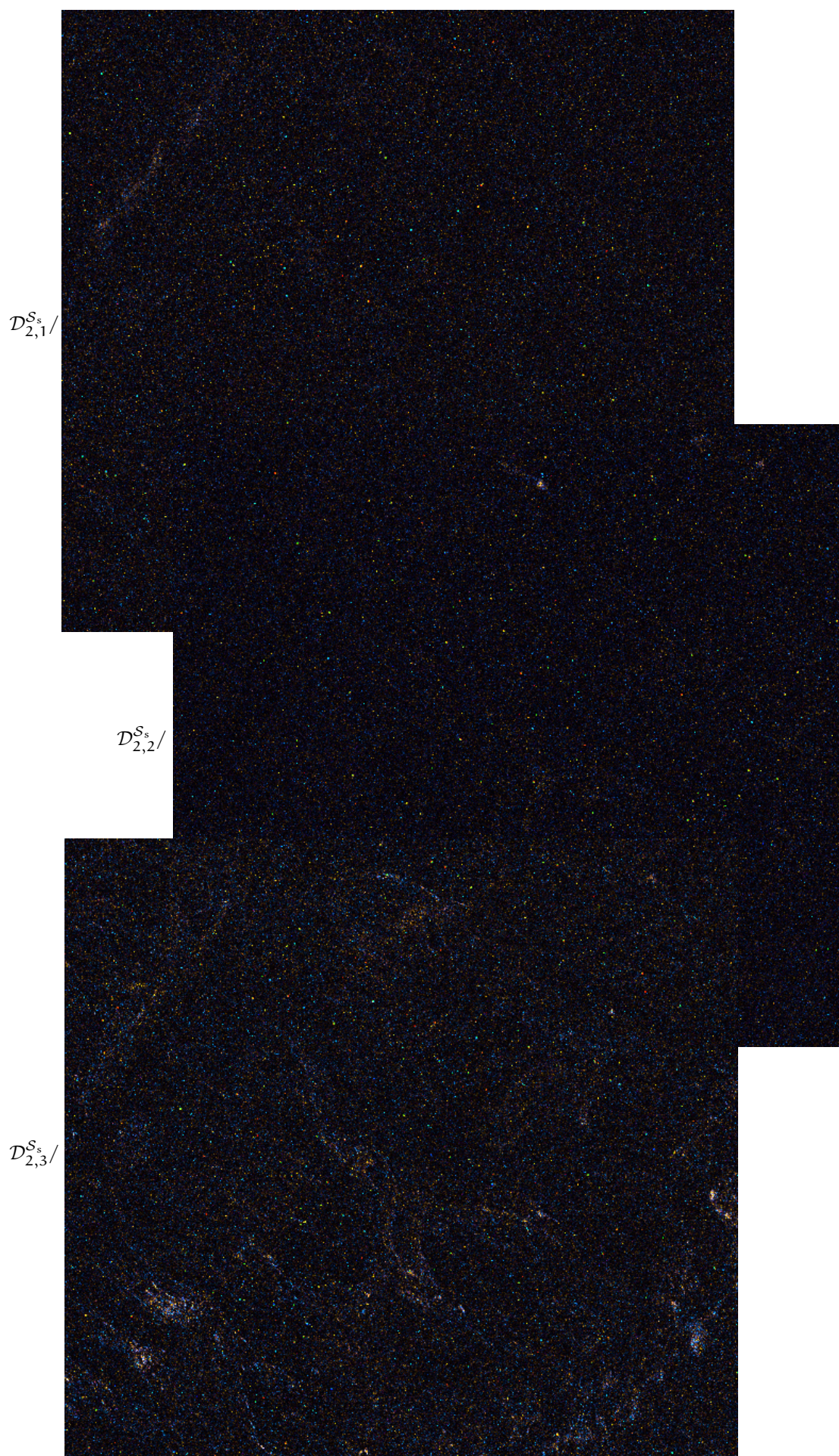


Fig. 11. Scalar sigmoid shrinkage D^{S_s} of geometric wavelet change-images given in Figure 10.

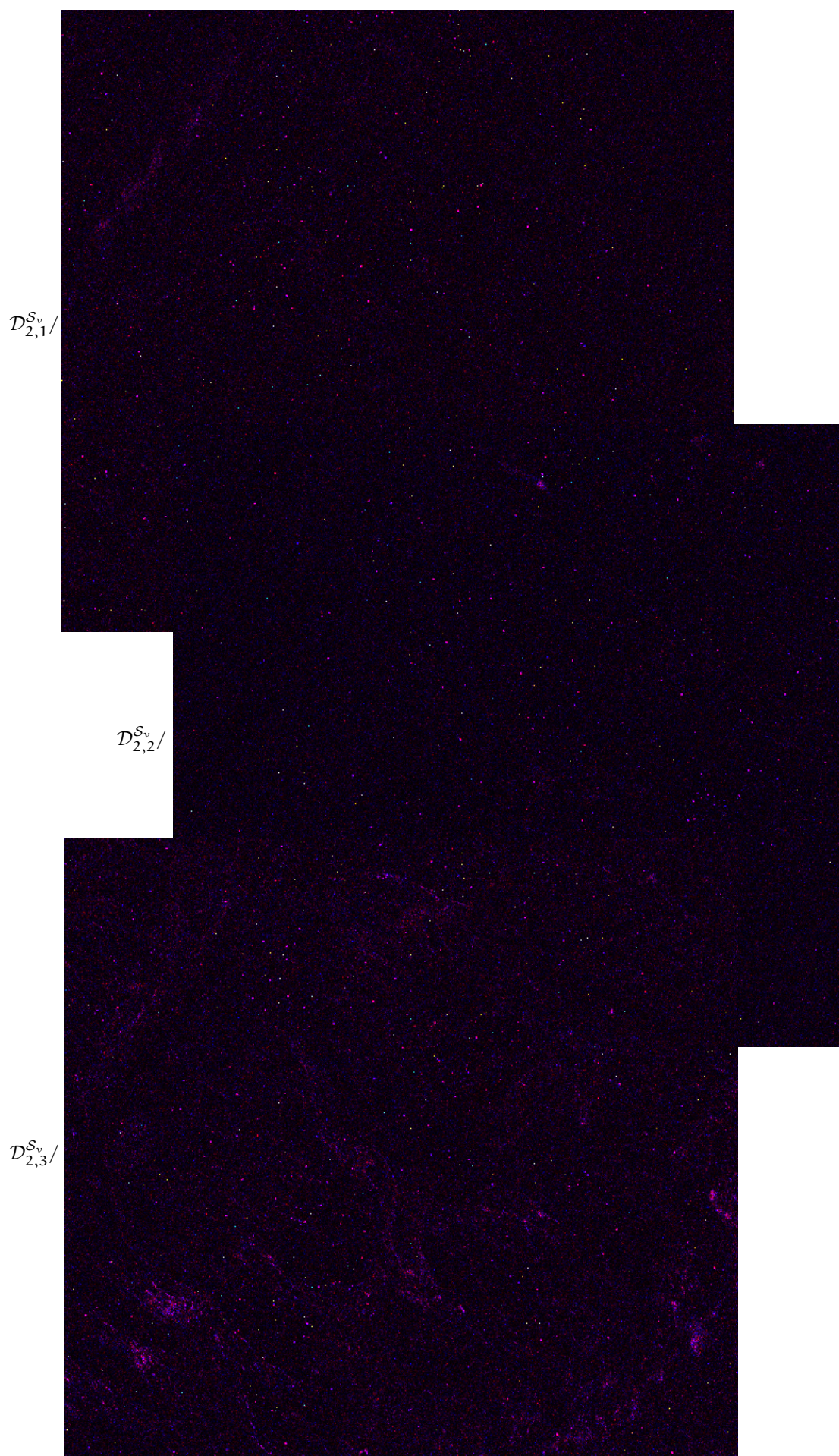


Fig. 12. Vector sigmoid shrinkage D^{S_v} of geometric wavelet change-images given in Figure 10.

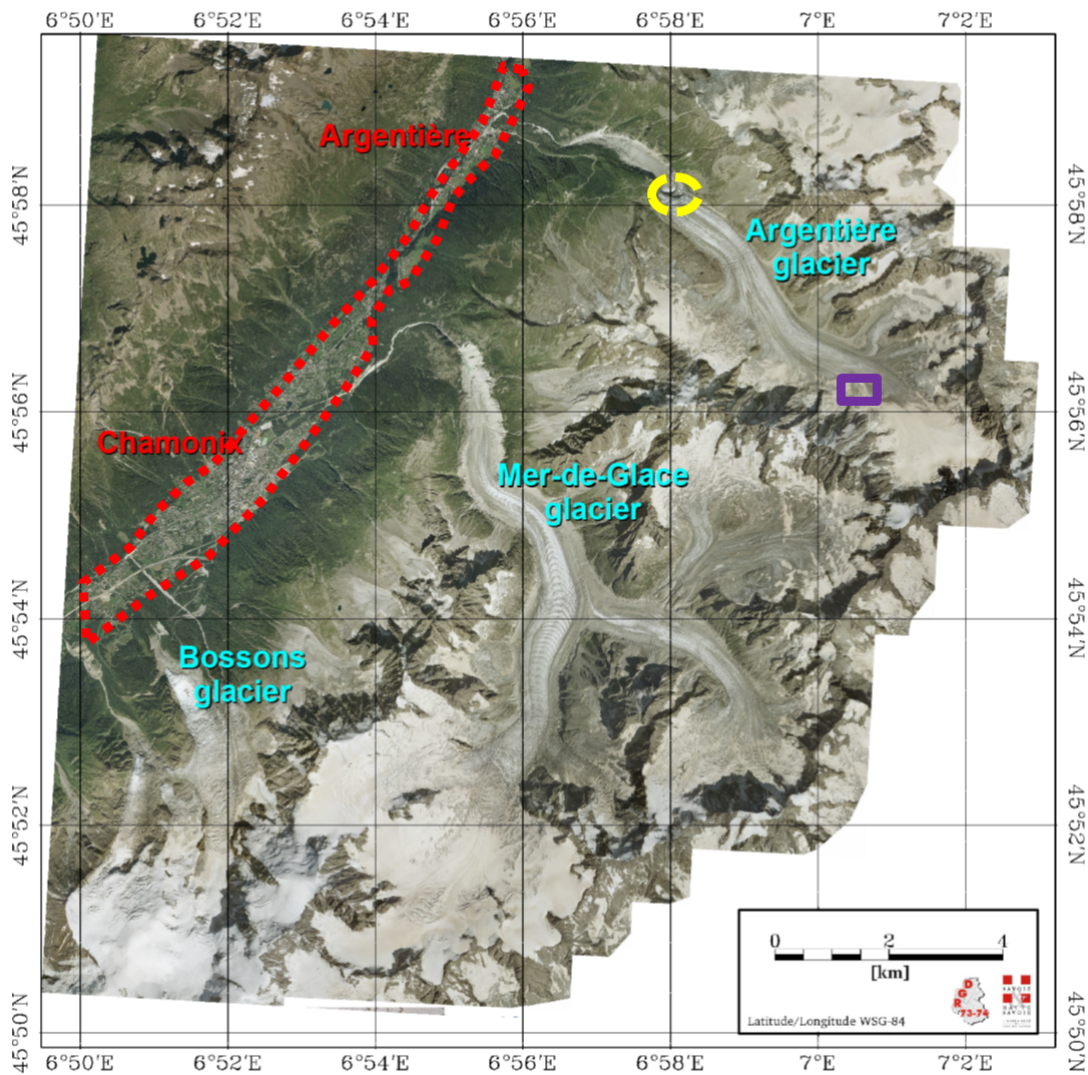


Fig. 13. Localization of level-2 geometric changes over Chamonix-Mont Blanc test site. Most important changes concern 2 zones that are known to be dynamic: the urban area (Chamonix valley, in red-dotted) and a serac fall area (in yellow-dashed). Changes also occur on a specific zone near the Argentière glacier accumulation area (magenta-square-box, probably a change due to an avalanche). See Figure 12 for identifying the dates and the amplitudes of the changes.

geometric approximation and differencing operators. Sparsity and stochasticity properties of additive (arithmetic) and multiplicative (geometric) wavelet transforms have been provided and illustrated on a multiplicative observation models.

In the multiplicative noise model, the paper has shown that:

- concerning sparsity, additive detail wavelet coefficients are impacted by the presence of signals (large amounts of signal contribution in detail coefficients), whereas few signal contributions occur in multiplicative detail coefficients.
- concerning stochasticity, geometric wavelets inherit stationary properties of the input noise whereas additive stationary noise becomes non-stationary in the additive wavelet domain, due to the impact of noise-free signals in detail coefficients.

Moreover, the paper has shown that the statistical properties of geometric wavelets makes them good candidates for the analysis of SAR image time series: in contrast to additive wavelets change-images, geometric wavelet ones are not affected by the presence of trends in the noise-free signal. Change analysis in time series can thus be performed by using block shrinkage on geometric wavelet coefficients, resulting in fast and accurate spatio-temporal change detection and joint regularization.

REFERENCES

- [1] H. Xie, L. E. Pierce, and F. T. Ulaby, "Statistical properties of logarithmically transformed speckle," *IEEE Transactions on Geoscience and Remote Sensing*, vol. 40, no. 3, pp. 721 – 727, Mar. 2002.
- [2] R. Garcia, T. Nicosevici, and X. Cufi, "On the way to solve lighting problems in underwater imaging," in *OCEANS '02 MTS/IEEE*, vol. 2, 2002, pp. 1018–1024 vol.2.

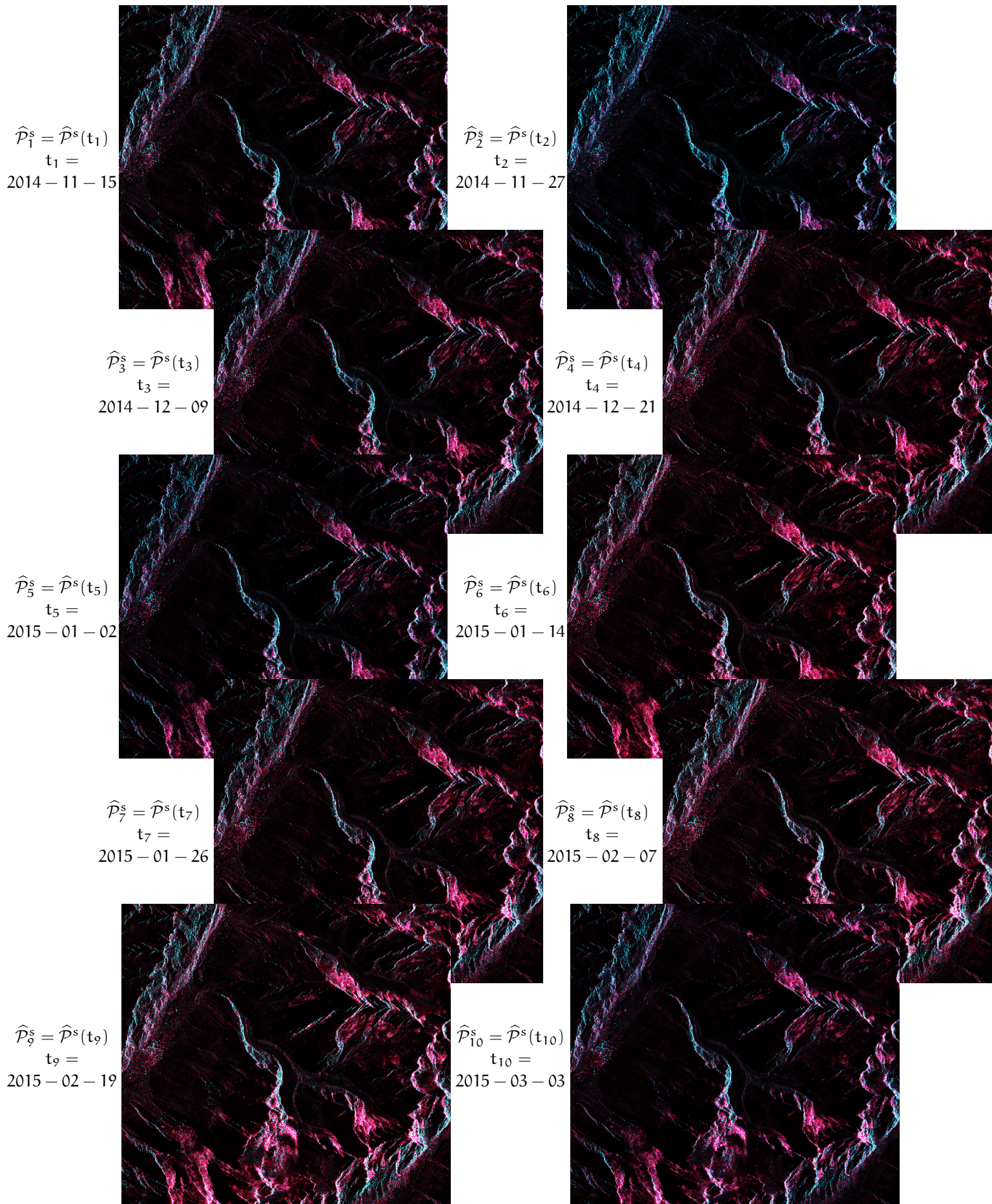


Fig. 14. Scalar sigmoid geometric wavelet regularization of Sentinel-1A dual PolSAR image time series of Figure 9.

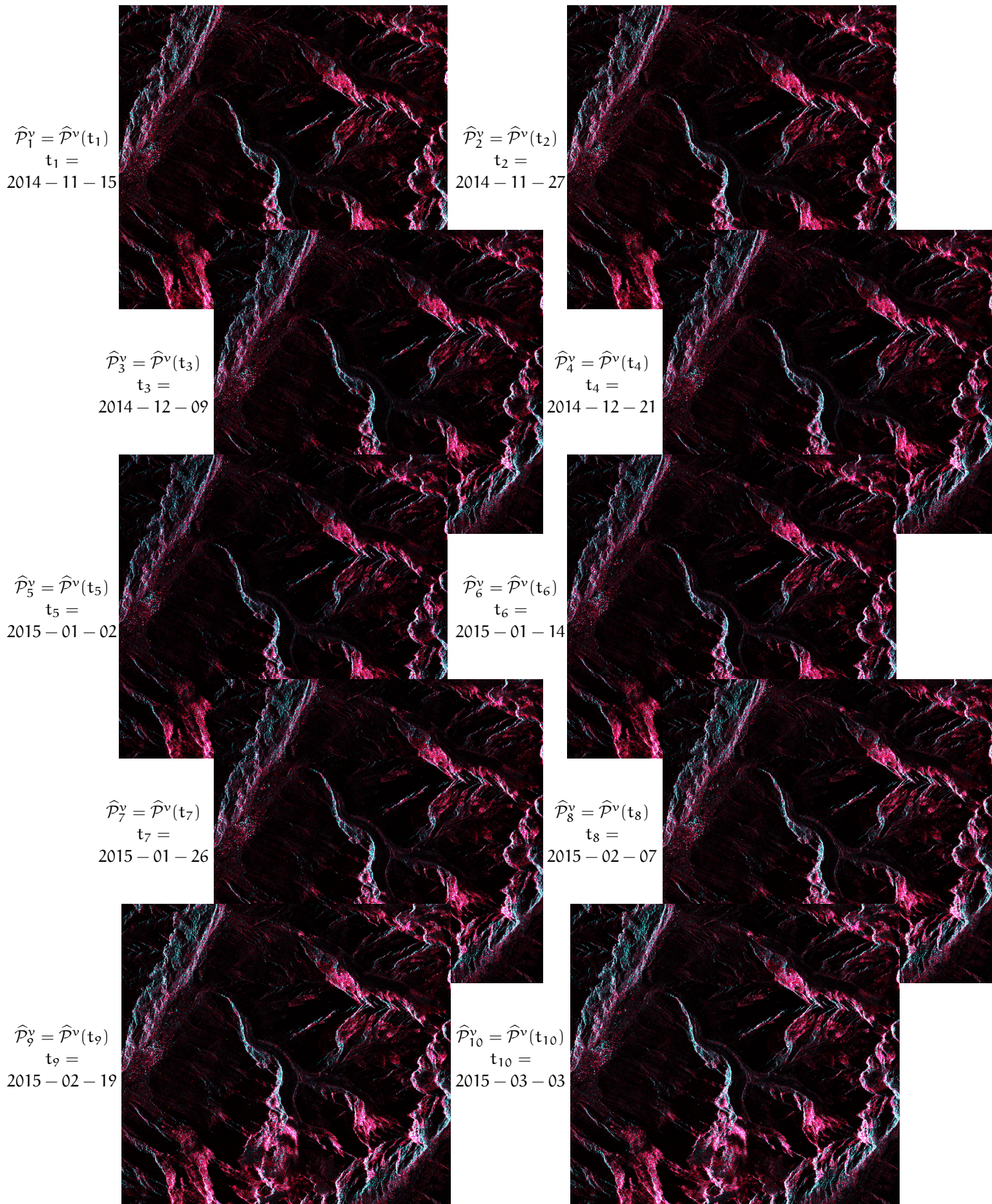


Fig. 15. Vector sigmoid geometric wavelet regularization of Sentinel-1A dual PolSAR image time series of Figure 9.

- [3] O. Michailovich and A. Tannenbaum, "Despeckling of medical ultrasound images," *Ultrasonics, Ferroelectrics and Frequency Control, IEEE Transactions on*, vol. 53, no. 1, pp. 64–78, 2006.
- [4] L. Florack and H. Assen, "Multiplicative calculus in biomedical image analysis," *Journal of Mathematical Imaging and Vision*, vol. 42, no. 1, pp. 64–75, 2012. [Online]. Available: <http://dx.doi.org/10.1007/s10851-011-0275-1>
- [5] P. Gould and F. Vahid-Araghi, "Time series with multiple seasonal patterns," in *Forecasting with Exponential Smoothing*, ser. Springer Series in Statistics. Springer Berlin Heidelberg, 2008, pp. 229–254. [Online]. Available: http://dx.doi.org/10.1007/978-3-540-71918-2_14
- [6] M. Verbeek, *A Guide to Modern Econometrics, 4th Edition*. John Wiley & Sons, February 2012.
- [7] J. M. Box-Steffensmeier and C. J. W. Zorn, "Duration models and proportional hazards in political science." Springer Berlin Heidelberg, 2001, vol. 45, no. 4, pp. 972–988.
- [8] C. Marin, F. Bovolo, and L. Bruzzone, "Building change detection in multitemporal very high resolution SAR images," *IEEE Trans. Geosci. Remote Sens.*, vol. 53, no. 5, pp. 2664–2682, 2015.
- [9] W. Yang, H. Song, G.-S. Xia, and C. Lopez-Martinez, "Dissimilarity measurements for processing and analyzing PolSAR data: A survey," in *Proc. IGARSS Milan, Italy*, pp. 1562–1565, 2015.
- [10] G. Quin, B. Pinel-Puysségur, J.-M. Nicolas, and P. Loreaux, "MIMOSA: An automatic change detection method for SAR time series," *IEEE Trans. Geosci. Remote Sens.*, vol. 52, no. 9, pp. 5349–5363, 2014.
- [11] G. Liu and H. Zhong, "Nonlocal means filter for polarimetric SAR despeckling based on discriminative similarity measure," *IEEE Geosci. Remote Sens. Lett.*, vol. 11, no. 2, pp. 514–518, 2014.
- [12] A. C. Frery, A. D. C. Nascimento, and R. J. Cintra, "Analytic expressions for stochastic distances between relaxed complex Wishart distributions," *IEEE Trans. Geosci. Remote Sens.*, vol. 52, no. 2, pp. 1213–1226, 2014.
- [13] A. M. Atto, E. Trouvé, Y. Berthoumieu, and G. Mercier, "Multitask divergence matrices for the analysis of sar image time series," *IEEE Transactions on Geoscience and Remote Sensing*, vol. 51, no. 4, pp. 1922–1938, April 2013. [Online]. Available: <http://dx.doi.org/10.1109/TGRS.2012.2210228>
- [14] M. Dabboor, M. J. Collins, V. Karathanassi, and A. Braun, "An unsupervised classification approach for polarimetric SAR data based on the Chernoff distance for complex Wishart distribution," *IEEE Trans. Geosci. Remote Sens.*, vol. 51, no. 7, pp. 4200–4213, 2013.
- [15] G. Quin, B. Pinel-Puysségur, and J.-M. Nicolas, "Comparison of harmonic, geometric and arithmetic means for change detection in SAR time series," *EUSAR*, 2012.
- [16] E. Trouvé, Y. Chambenoit, N. Classeau, and P. Bolon, "Statistical and operational performance assessment of multitemporal SAR image filtering." *IEEE Trans. Geosci. Remote Sens.*, vol. 41, no. 11, pp. 2519–2530, 2003.
- [17] R. Touzi, "A review of speckle filtering in the context of estimation theory," *IEEE Trans. Geosci. Remote Sens.*, vol. 40, no. 11, p. 2392–2404, 2002.
- [18] A. Gar-OnYeh and Z. Qi, *Space-Time Integration in Geography and GIScience. Chapter 19: Short-Interval Monitoring of Land Use and Land Cover Change Using a Time Series of RADARSAT-2 Polarimetric SAR Images*. Springer Link, 2015.
- [19] X. Su, C. Deledalle, F. Tupin, and H. Sun, "Two-step multitemporal nonlocal means for synthetic aperture radar images," *IEEE Trans. Geosci. Remote Sens.*, vol. 52, no. 10, pp. 6181–6196, 2014.
- [20] V. Akbari, A. P. Doulgeris, and T. Eltoft, "Monitoring glacier changes using multitemporal multipolarization SAR images," *IEEE Trans. Geosci. Remote Sens.*, vol. 52, no. 6, pp. 3729–3741, 2014.
- [21] T. T. Lê, A. M. Atto, E. Trouvé, and J.-M. Nicolas, "Adaptive multitemporal sar image filtering based on the change detection matrix," *IEEE Geoscience and Remote Sensing Letters*, vol. 11, no. 10, pp. 1826–1830, Oct 2014.
- [22] T. Schellenberger, B. Ventura, M. Zebisch, and C. Notarnicola, "Wet snow cover mapping algorithm based on multitemporal COSMO-SkyMed X-band SAR images," *IEEE J. Sel. Topics Appl. Earth Observations Remote Sens.*, vol. 5, no. 3, pp. 1045–1053, 2012.
- [23] X. Xing, Z. Chen, H. Zou, and S. Zhou, "Statistical assessment of model fit for SAR sea clutter," in *Proc. SPIE*, vol. 7494, 2009.
- [24] S. Quegan, T. L. Toan, J. J. Y. Jiong, F. Ribbes, and N. Floury, "Multitemporal ERS SAR analysis applied to forest mapping," *IEEE Trans. Geosci. Remote Sens.*, vol. 38, no. 2, pp. 741–753, 2000.
- [25] J. Lehtiranta, S. Siirila, and J. Karvonen, "Comparing C- and L-band SAR images for sea ice motion estimation," *The Cryosphere*, vol. 9, pp. 357–366, 2015.
- [26] A. Alonso-Gonzalez, C. Lopez-Martinez, and P. Salembier, "Filtering and segmentation of polarimetric SAR data based on binary partition trees," *IEEE Trans. Geosci. Remote Sens.*, vol. 50, no. 2, pp. 593–605, 2012.
- [27] D. Amitrano, F. Ciervo, P. D. Bianco, G. D. Martino, A. Iodice, F. Mitidieri, D. Riccio, G. Ruello, M. N. Papa, and Y. Kousoube, "Monitoring soil erosion and reservoir sedimentation in semi-arid region through remote sensed SAR data: A case study in Yatenga region, Burkina Faso," *Engineering Geology for Society and Territory*, vol. 3, pp. 539–542, 2015.
- [28] H. Zhong, Y. Li, and L. Jiao, "SAR image despeckling using bayesian nonlocal means filter with sigma preselection," *IEEE Geosci. Remote Sens. Lett.*, vol. 8, no. 4, pp. 809–813, 2011.
- [29] S. Parrilli, M. Poderico, C. V. Angelino, and L. Verdoliva, "A nonlocal SAR image denoising algorithm based on LLMSE wavelet shrinkage," *IEEE Trans. Geosci. Remote Sens.*, vol. 50, no. 2, pp. 606–616, 2012.
- [30] A. M. Atto, D. Pastor, and G. Mercier, "Wavelet shrinkage: Unification of basic thresholding functions and thresholds," *Signal, Image and Video Processing, Springer*, vol. 5, no. 1, pp. 11–28, 2011. [Online]. Available: <http://dx.doi.org/10.1007/s11760-009-0139-y>
- [31] E. J. Candès and D. L. Donoho, "Curvelets - a surprisingly effective nonadaptive representation for objects with edges," *Curves and Surfaces, L. L. Schumaker et al. (eds), Vanderbilt University Press, Nashville, TN*, 2000.
- [32] —, "New tight frames of curvelets and optimal representations of objects with piecewise C^2 singularities," *Communications on Pure and Applied Mathematics, Wiley Periodicals, Inc., A Wiley Company*, vol. 57, no. 2, pp. 219–266, 2004.
- [33] E. Candès, L. Demanet, D. Donoho, and L. Ying, "Fast discrete curvelet transforms," *Multiscale Modeling and Simulation*, vol. 5, no. 3, pp. 861–899, 2006.
- [34] G. Peyré, C. Dossal, E. L. Pennec, and S. Mallat, "Geometric estimation with orthogonal bandlet bases," in *Proceedings of SPIE Wavelet XII*, 2007.
- [35] S. Mallat, *A wavelet tour of signal processing, second edition*. Academic Press, 1999.
- [36] I. Daubechies, *Ten lectures on wavelets*. SIAM, Philadelphia, PA, 1992.
- [37] A. M. Atto and Y. Berthoumieu, "Wavelet packets of nonstationary random processes: Contributing factors for stationarity and decorrelation," *IEEE Transactions on Information Theory*, vol. 58, no. 1, Jan. 2012. [Online]. Available: <http://dx.doi.org/10.1109/TIT.2011.2167496>
- [38] R. R. Coifman and D. L. Donoho, *Translation invariant denoising*. Lecture Notes in Statistics, 1995, no. 103, pp. 125–150.
- [39] X. Hou, J. Yang, G. Jiang, and X. Qian, "Complex sar image compression based on directional lifting wavelet transform with high clustering capability," *Geoscience and Remote Sensing, IEEE Transactions on*, vol. 51, no. 1, pp. 527–538, 2013.

- [40] J. Ranjani and S. Thiruvengadam, "Dual-tree complex wavelet transform based sar despeckling using interscale dependence," *Geoscience and Remote Sensing, IEEE Transactions on*, vol. 48, no. 6, pp. 2723-2731, 2010.
- [41] D. L. Donoho and I. M. Johnstone, "Ideal spatial adaptation by wavelet shrinkage," *Biometrika*, vol. 81, no. 3, pp. 425 - 455, Aug. 1994.
- [42] T. T. Lê, A. M. Atto, and E. Trouvé, "Change analysis of dual polarimetric sentinel-1 sar image time series using stationary wavelet transform and change detection matrix," *8th International Conference on the Analysis of Multitemporal Remote Sensing Images, Annecy, France, July 22 - 24*.

APPENDIX A

PROOF OF PROPOSITION 2

By considering the log of $\mathbf{C}_{j+1,2n+\epsilon}^\times$ denoted by $\mathbf{D}_{j+1,2n+\epsilon}$, we are concerned by an additive combinations of $\mathbf{D}_{j,n} = \log \mathbf{C}_{j,n}^\times$.

The autocorrelation functions

$$R_{\mathbf{D}_{j+1,2n+\epsilon}}[k, \ell] = \mathbb{E} \mathbf{D}_{j+1,2n+\epsilon}[k] \mathbf{D}_{j+1,2n+\epsilon}[\ell]$$

and

$$R_{\mathbf{D}_{j,n}}[k, \ell] = \mathbb{E} \mathbf{D}_{j,n}[k] \mathbf{D}_{j,n}[\ell]$$

of $\mathbf{D}_{j+1,2n+\epsilon}$ and $\mathbf{D}_{j,n}$ satisfy the relation:

$$R_{\mathbf{D}_{j+1,2n+\epsilon}}[k, \ell] = \sum_{p \in \mathbb{Z}} \sum_{q \in \mathbb{Z}} \mathbf{h}_\epsilon[p - 2k] \mathbf{h}_\epsilon[q - 2\ell] \times R_{\mathbf{D}_{j,n}}[p, q] \quad (36)$$

Since $\mathbf{D}_{j,n}$ is stationary: $R_{\mathbf{D}_{j,n}}[p, q] \triangleq R_{\mathbf{D}_{j,n}}[p - q]$, then Eq. (36) can be rewritten in the form

$$R_{\mathbf{D}_{j+1,2n+\epsilon}}[k, \ell] = \sum_{p \in \mathbb{Z}} R_{\mathbf{D}_{j,n}}[p] \times \sum_{q \in \mathbb{Z}} \mathbf{h}_\epsilon[p + q - 2k] \mathbf{h}_\epsilon[q - 2\ell]. \quad (37)$$

By taking into account that (Parseval's theorem):

$$\begin{aligned} \sum_{q \in \mathbb{Z}} \mathbf{h}_\epsilon[p + q - 2k] \mathbf{h}_\epsilon[q - 2\ell] &= \\ \sum_{q \in \mathbb{Z}} \tau_{2k-2\ell-p} \mathbf{h}_\epsilon[q] \mathbf{h}_\epsilon[q] &= \\ = \frac{1}{2\pi} \int_{-\pi}^{\pi} \left| \widehat{\mathbf{H}}_\epsilon(\omega) \right|^2 e^{i(2k-2\ell-p)\omega} d\omega, \end{aligned} \quad (38)$$

we obtain from Eq. (37):

$$R_{\mathbf{D}_{j+1,2n+\epsilon}}[k, \ell] = \frac{1}{2\pi} \int_{-\pi}^{\pi} e^{i(2k-2\ell)\omega} \left| \widehat{\mathbf{H}}_\epsilon(\omega) \right|^2 \times \left(\sum_{p \in \mathbb{Z}} R_{\mathbf{D}_{j,n}}[p] e^{-ip\omega} \right) d\omega \quad (39)$$

The proof follows from Eq. (23) and Eq. (39), by identifying the Fourier expansion of $\gamma_{\mathbf{D}_{j,n}}$ in Eq. (39) and

by noting that $R_{\mathbf{D}_{j+1,2n+\epsilon}}[p, q] \triangleq R_{\mathbf{D}_{j+1,2n+\epsilon}}[p - q] = R_{\mathbf{D}_{j+1,2n+\epsilon}}[m]$ where $m = k - \ell$.

APPENDIX B

PROOF OF PROPOSITION 3

Let $\epsilon \in \{0, 1\}$. The Haar scaling filter $\mathbf{H}_0^{\text{Haar}}$ and wavelet filter $\mathbf{H}_1^{\text{Haar}}$ satisfies

$$\mathbf{H}_\epsilon^{\text{Haar}}(\omega) = \frac{1}{2} (1 + (1 - 2\epsilon)e^{-i\omega}) \quad (40)$$

By taking into account Eqs. (5) and (40), we have

$$\mathbf{H}_{j,n}^{\text{Haar}}(\omega) = 2^{-j/2} \prod_{\ell=1}^j (1 + (1 - 2\epsilon_\ell)e^{-i\omega}). \quad (41)$$

Thus,

$$\left| \mathbf{H}_{j,n}^{\text{Haar}}(\omega) \right|^2 = \prod_{\ell=1}^j (1 + (1 - 2\epsilon_\ell) \cos(2^{\ell-1}\omega)). \quad (42)$$

The proof follows by noting that $(1 - 2\epsilon_\ell) \cos(2^{\ell-1}\omega) = \cos(2^{\ell-1}\omega + \epsilon_\ell\pi)$ after some straightforward simplifications by using trigonometry double angle properties.

APPENDIX C

PROOF OF PROPOSITION 4

From a change of variable in Eq. (29), we obtain

$$R_{\mathbf{D}_{j,0}^{\text{Haar}}}[m] = \frac{1}{\pi} \int_0^{2^j\pi} \left(\frac{\text{sinc}(\omega/2)}{\text{sinc}(\omega/2^{j+1})} \right)^2 \gamma_{\mathbf{Y}}\left(\frac{\omega}{2^j}\right) \cos m\omega d\omega.$$

First, we observe that:

$$\left| R_{\mathbf{D}_{j,0}^{\text{Haar}}}[m] \right| \leq \|\gamma_{\mathbf{Y}}\|_\infty \times \left(\frac{1}{\pi} \int_0^{2^j\pi} \left(\frac{\text{sinc}(\omega/2)}{\text{sinc}(\omega/2^{j+1})} \right)^2 d\omega \right).$$

and, furthermore, we have

$$\frac{1}{\pi} \int_0^{+\infty} \left(\frac{\text{sinc}(\omega/2)}{\text{sinc}(\omega/2^{j+1})} \right)^2 d\omega = 1.$$

In this respect, we derive

$$\left| R_{\mathbf{D}_{j,0}^{\text{Haar}}}[m] \right| \leq \|\gamma_{\mathbf{Y}}\|_\infty$$

so that, from the Lebesgue dominated convergence theorem,

$$\lim_{j \rightarrow +\infty} R_{\mathbf{D}_{j,0}^{\text{Haar}}}[m] = \gamma_{\mathbf{Y}}(0) \frac{1}{\pi} \int_0^{+\infty} (\text{sinc}(\omega/2))^2 \cos m\omega d\omega$$

Proposition 4 then follows by noting that

$$\int_0^{+\infty} (\text{sinc}(\omega/2))^2 \cos m\omega d\omega = \pi\delta[m]$$